Monthly Notices
of the
ROYAL ASTRONOMICAL SOCIETY

MNRAS **483,** 3146–3167 (2019)
Advance Access publication 2018 November 10

doi:10.1093/mnras/sty3053

The RMS survey: Ammonia mapping of the environment of young massive stellar objects – II★

S. J. Billington [1]†, J. S. Urquhart [1], C. Figura,[2] D. J. Eden [3] and T. J. T. Moore[3]

[1]*Centre for Astrophysics and Planetary Science, University of Kent, Canterbury CT2 7NH, UK*
[2]*Wartburg College, Waverly, IA 50677, USA*
[3]*Astrophysics Research Institute, Liverpool John Moores University, IC2, Liverpool Science Park, 146 Brownlow Hill, Liverpool L3 5RF, UK*

Accepted 2018 November 7. Received 2018 November 07; in original form 2018 September 7

ABSTRACT

We present the results from NH_3 mapping observations towards 34 regions identified by the Red MSX Source (RMS) survey. We have used the Australia Telescope Compact Array to map ammonia (1, 1) and (2, 2) inversion emission spectra at a resolution of 10 arcsec with velocity channel resolution of 0.4 km s^{-1} towards the positions of embedded massive star formation. Complementary data have been used from the ATLASGAL and GLIMPSE Legacy Surveys in order to improve the understanding of the regions and to estimate physical parameters for the environments. The fields have typical masses of $\sim$1000 $M_\odot$, radii of $\sim$0.15 pc, and distances of $\sim$3.5 kpc. Luminosities range between $\sim10^3$ and $\sim10^6$ $L_\odot$ and kinetic temperatures between 10 and 40 K. We classify each field into one of two subsets in order to construct an evolutionary system for massive star formation in these regions based on the morphology and relative positions of the NH_3 emission, RMS sources, and ATLASGAL thermal dust emission. Differences in morphology between NH_3 emission and ATLASGAL clumps are shown to correspond to evolutionary stages of ongoing massive star formation in these regions. The study has been further refined by including the positions of known methanol and water masers in the regions to gain insight into possible protostellar regions and triggered star formation.

Key words: stars: evolution – stars: massive – ISM: general.

1 INTRODUCTION

Massive stars (>8 $M_\odot$) play a vital role in the evolution of the Galaxy due to their powerful outflows, strong stellar winds, large amounts of UV radiation, and chemical enrichment of material of the interstellar medium (ISM). These feedback processes can have a dramatic impact on the local environment by changing the chemistry and injecting huge amounts of energy into the ISM. They are also responsible for driving strong shocks into the surrounding molecular clouds, which can have a direct effect on future generations of stars through the compression and subsequent collapse of molecular structures often referred to as triggering (e.g. Urquhart et al. 2007; Deharveng et al. 2010; Thompson et al. 2012), or by disrupting clouds before the star formation has begun. Massive stars therefore play an important role in regulating future generations of stars and driving the evolution of their host galaxies (Kennicutt 2005).

Even though massive stars have a profound influence on the Universe, our knowledge and understanding of how these celestial objects form is still fairly poor for a number of reasons. Massive stars form almost exclusively in compact OB clusters or large OB associations, making it difficult to differentiate between the properties of a single star and the cluster itself. Their relative rarity compared to lower mass stars results in regions of high-mass star formation being located at greater distances (generally farther than a few kpc away), exacerbating source confusion. Furthermore, these objects evolve rapidly (their Kelvin–Helmholtz time-scale is much shorter than their free-fall collapse timescale). They reach the main sequence while still deeply embedded in their natal cloud, so the earliest stages in their evolution take place behind many hundreds of magnitudes of visual extinction and can only be studied at far-infrared and submillimetre wavelengths.

Two of the earliest stages in the formation of OB stars are massive young stellar objects (MYSOs; Lumsden et al. 2013) and the compact H II regions (Wood & Churchwell 1989; Kurtz, Churchwell & Wood 1994; Urquhart et al. 2013b). During the MYSO stage the newly formed protostar begins to heat up its envelope and becomes detectable at mid-infrared wavelengths. This stage ends when the star joins the main sequence and begins to ionize its natal molecular

★ The full version of Tables 3 and 6 are only available in electronic form at the CDS via anonymous ftp to cdsarc.u-strasbg.fr (130.79.125.5) or via http://cdsweb.u-strasbg.fr/cgi-bin/qcat?J/MNRAS/.

† E-mail: sjbb2@kent.ac.uk

cloud, leading to the creation of an ultra compact H II region. Both of these stages are physically distinct from the earlier hot molecular core stage, which is generally not detectable at mid-infrared wavelengths (De Buizer et al. 2002).

The Red MSX Source (RMS) survey (Lumsden et al. 2013) has identified ∼3000 MYSOs and H II region candidates located throughout the Galactic plane. These sources were initially identified from their mid-infrared colours using the MSX point source catalogue (Price et al. 2001) and 2MASS data (Cutri et al. 2003). The nature of these candidates was later confirmed through an extensive multiwavelength follow-up campaign (e.g. Mottram et al. 2007; Urquhart et al. 2007a,b; Urquhart et al. 2008; Urquhart, Morgan & Thompson 2009a; Urquhart et al. 2009b, 2011; Cooper et al. 2013). This survey has identified ∼1700 MYSOs and H II regions and is the largest and most well-characterized catalogue of these stages of massive star formation that has been compiled with determined distances (Urquhart et al. 2012, 2014b) and luminosities (Mottram et al. 2011a,b; Urquhart et al. 2014b) and is an order of magnitude larger than any previous study. The RMS catalogue sample is therefore an ideal starting point for more detailed studies of these massive star forming regions.

This is the second RMS paper that used ammonia mapping observations to investigate the structure and properties of high-mass star forming clumps. The first paper (Urquhart et al. 2015a; hereafter Paper I) followed up 66 high-mass star-forming clumps with the Green Bank Telescope (GBT) with an angular resolution of ∼30 arcsec. In this paper we present ammonia observations towards another 34 massive star-forming regions located in the fourth quadrant. This subsample of MYSOs and H II regions drawn from the RMS survey has been mapped using the lowest inversion emission spectra of interstellar ammonia [i.e. NH_3 $(J, K) = (1, 1)$ and $(2, 2)$]. Ammonia does not deplete from the gas phase in the cold ($T \sim 10$–40 K; Ho et al. 1983; Mangum, Wootten & Mundy 1992) and high-density ($n > 10^4$ cm^{-3}) conditions that are typical (20–30 K; Urquhart et al. 2011; Paper I) of these natal clumps, making it an excellent probe of the physical conditions at this stage of star formation.

Ammonia observations have been used by the H_2O Southern Galactic Plane Survey (HOPS; Walsh et al. 2011; Purcell et al. 2012; Longmore et al. 2017) to map the distribution of dense star forming gas; other studies have used it to investigate the physical properties and kinematics of different kinds of star formation environments in the Galaxy, such as infrared dark clouds (e.g. Perault et al. 1996; Pillai et al. 2006; Ragan, Bergin & Wilner 2011; Chira et al. 2013) and high-mass star-forming regions (e.g. Dunham et al. 2011; Urquhart et al. 2011; Paper I). The main reason for the widespread use of ammonia transitions is that the hyperfine structure of the emission can be used to derive multiple free parameters allowing for an in-depth analysis of the kinematics, morphology, and thermodynamics of such regions.

The main aims of this study are to compare the physical properties of different stages of high-mass star formation and investigate how feedback from outflows and UV-radiation can affect the local environment as the embedded high-mass stars evolve. The structure of the paper is as follows: Section 2 outlines our sample selection along with archival data sets used to complement this study, in Section 3 we describe the observational setup and reduction procedures used to process the data. We outline the source extraction method used to identify sources and the classification system which has been applied in Section 4. We describe our spectral line analysis and fitting procedure and how the various physical parameters are derived in Section 5. In Section 6 we discuss the differences between the classification groups with respect to multiple parameters from the spectral line analysis and results reported by other surveys [(Methanol Multibeam (MMB) survey (Caswell 2010), HOPS and ATLASGAL (Schuller et al. 2009)] and also how the regions are being affected by their local environments. The study is then summarized and concluded in Section 7.

2 SAMPLE SELECTION

The sample selection for this study was based on RMS objects towards which both strong NH_3 (1, 1) and (2, 2) inversion transition emission has previously been detected. The observational data set along with data reduction techniques are outlined in Section 3. The majority of objects that were selected lie within the inner Galactic plane and so are complemented by a wealth of additional data provided by other surveys such as ATLASGAL, HOPS, GLIMPSE, and MMB. We have therefore taken complementary data from these Galactic surveys in order to improve the understanding of the surrounding environments for the regions that are presented herein.

2.1 ARCHIVAL DATA

2.1.1 GLIMPSE images

We have used images from the GLIMPSE Legacy Survey (Benjamin et al. 2003; Churchwell et al. 2009) in order to investigate the surrounding environments at mid-infrared wavelengths. Three-colour images have been created using data at IRAC 3.4, 4.5, and 8 μm wavelength bands from the *Spitzer Space Telescope* (Fazio et al. 1998).

These images are capable of revealing the position of embedded objects with respect to the ammonia emission, such as MYSOs and compact H II regions under investigation here. The 8 μm band is also sensitive to the emission from polycyclic aromatic hydrocarbons (PAHs) that have been excited by UV radiation of embedded or nearby H II regions, making it an excellent tracer of the boundaries between molecular and ionized gas (Urquhart et al. 2007). Additionally, Cyganowski et al. (2008) have used the 4.5 μm band images in order to create a catalogue of extended green objects. These objects have an excess of 4.5 μm emission, which is thought to be result of shock-excited H_2 $(v = 0 - 0)$ S(9, 10, 11) lines and/or CO $(v = 1 - 0)$ bandhead (Churchwell et al. 2009) associated with molecular outflows from MYSOs, and therefore considered to be a good indicators for ongoing massive star formation.

These mid-infrared images can therefore provide a useful overview of the position of the embedded MYSOs and H II regions, the structure of their host clumps and their local environment.

GLIMPSE images are presented throughout the paper, and for each region which lies within the GLIMPSE survey coverage, their corresponding RGB image is given in the appendix. The wavelengths used for the three-colour images are 8, 4.5, and 3.4 μm for the red, green, and blue channels, respectively.

The GLIMPSE images show a range of environments as shown in Fig. 1. The upper left panel presents a region with an offset H ii region, which appears to be affecting the nearby dense gas, while the rest of the field appears to be quiescent. This source highlights the distribution of 8 m emission produced by PAHs excited in the interaction layers between ionization fronts and molecular gas. The upper right panel shows a much more evolved region with a number of evolved background stars, which some diffuse extended emission.

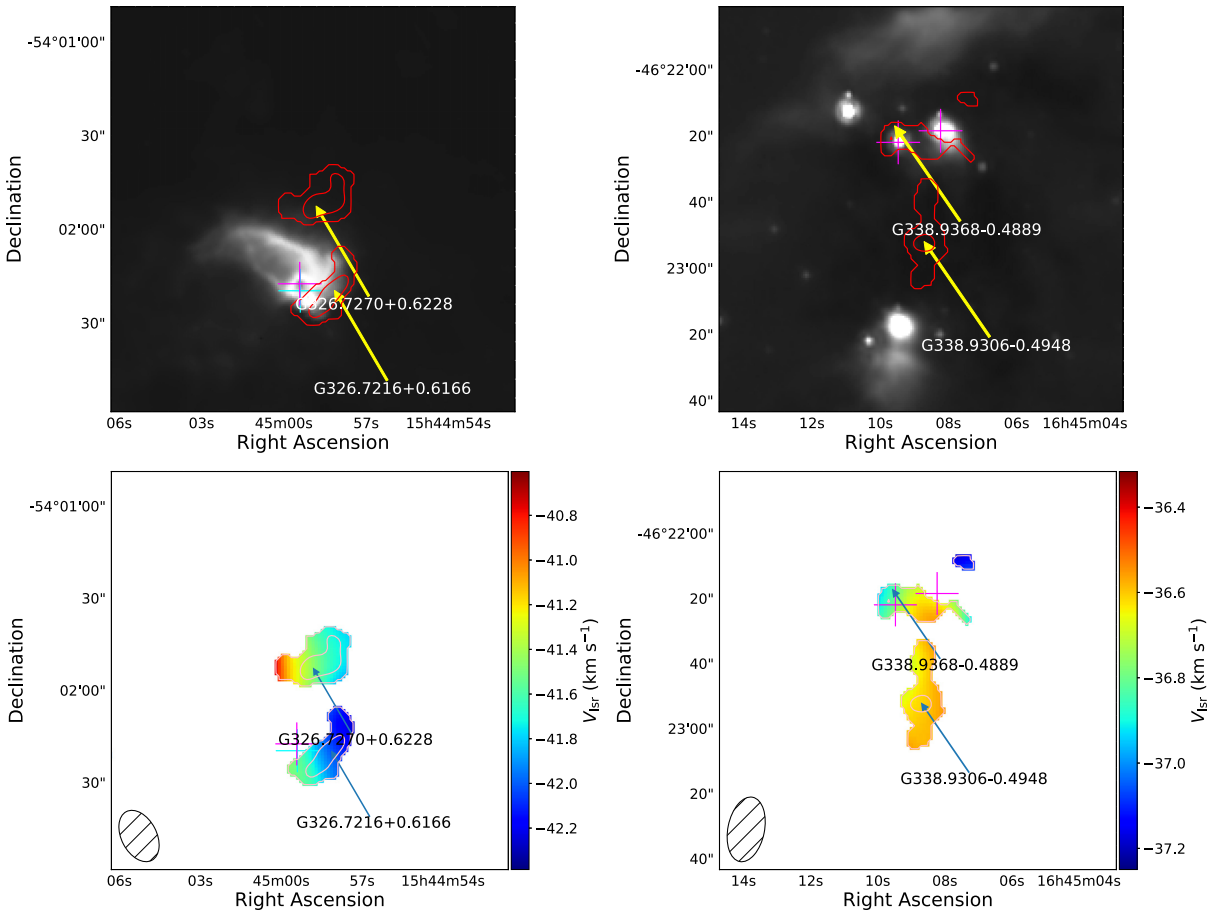

Figure 1. The upper panels present example 8 μm images taken from the GLIMPSE Legacy survey, while the lower panels show the velocity maps for the same regions. Magenta and cyan crosses mark the positions of any MYSOs or H II regions, respectively. NH_3 (1, 1) integrated emission contours are overplotted on both sets of images, the contours begin at 3σ and increase in steps of 0.5σ (values for σ/r.m.s. noise can be found in Table 2).

2.1.2 ATLASGAL dust emission

The APEX Large Area Survey of the Galaxy (ATLASGAL) survey (Schuller et al. 2009; Contreras et al. 2013; Csengeri et al. 2014) has surveyed 420 deg^2 of the Galactic plane, between $-80^\circ \leq \ell \leq +60^\circ$, and $-2^\circ \leq b \leq +1.5^\circ$ at 870 μm (345 GHz). ATLASGAL has traced dust emission across the Galactic plane and the compact source catalogue (CSC; Contreras et al. 2013; Urquhart et al. 2014a) produced from these maps consists of ∼10 000 compact clumps. The ATLASGAL survey covers 33 out of 34 of our observed fields (G261.6429−02.0922 lies outside of the ATLASGAL region). We have used emission contours overlaid onto the three-colour GLIMPSE images to compare the distribution of interstellar dust with the integrated ammonia emission and the mid-infrared environment for each observed field. These data are used to build a detailed picture of these star-forming environments and examine their physical properties, such as clump mass and luminosity (see Urquhart et al. 2018 for details of how these parameters are determined).

The clump masses and luminosities for 32 of the 33 fields covered by ATLASGAL range between $\sim 10^{2.5}$–10^4 M$_\odot$ and $\sim 10^3$–10^6 L$_\odot$, respectively. Although G286.2086 + 00.1694 is located in the ATLASGAL region it was not included in the study by Urquhart et al. (2018) and so the luminosity and clump masses were not available. These extracted data complement the sample by providing masses and luminosities of the entire regions as opposed to the small, denser substructures mapped by the NH_3 emission. The extracted parameters for each region can be found in Table 1.

2.1.3 Methanol MultiBeam survey

The MMB survey (Green et al. 2009) is an unbiased survey of the Galactic plane for 6668 MHz methanol masers. The coverage for the survey is $186^\circ \leq \ell \leq 60^\circ$ with the majority of detections found between $|b| \leq 1^\circ$. This species of astronomical maser is one of the most frequently detected, and is considered to be exclusively associated with the early stages of high-mass star formation (e.g. Minier et al. 2003). Comparison between the MMB catalogue and the ATLASGAL CSC (Urquhart et al. 2013a) and a set of dedicated dust continuum observations (Urquhart et al. 2015b) found that 99 per cent of methanol masers are associated with dense star-forming clumps. There is an MMB source present in 20 of the 34 fields observed (∼59 per cent).

2.1.4 HOPS

The HOPS (Walsh et al. 2011) has mapped 100 square degrees of the southern Galactic plane, between $290^\circ \leq \ell \leq 30^\circ$ and $|b| \leq 0.5^\circ$, at 19.5–27.5 GHz. They have detected over 540 groups of H_2O masers in this region, which have been followed up at high resolution with the ATCA to get accurate positions (<1 arcsec; Walsh et al. 2014).

Table 1. Extracted field parameters from the ATLASGAL survey.

Field id	Field name	log(L_{bol}) ($L_\odot$)	log(M_{field}) ($M_\odot$)	log[$N(H_2)$] (cm^{-2})
1	G261.6429 − 02.0922	–	–	–
2	G286.2086 + 00.1694	–	–	–
3	G305.2017 + 00.2072	5.139	3.527	23.362
4	G309.4230 − 00.6208	3.327	3.075	22.810
5	G312.5963 + 00.0479	4.827	3.175	22.836
6	G314.3197 + 00.1125	4.077	3.176	22.748
7	G318.9480 − 00.1969	3.871	2.523	23.092
8	G322.1729 + 00.6442	5.466	3.736	23.416
9	G323.4584 − 00.0787	5.074	3.106	22.873
10	G326.4755 + 00.6947	3.733	2.926	23.513
11	G326.7249 + 00.6159	4.545	2.686	23.079
12	G327.3941 + 00.1970	3.938	3.246	22.928
13	G327.4014 + 00.4454	4.761	3.587	23.321
14	G328.2523 − 00.5320	4.665	3.597	23.310
15	G328.3067 + 00.4308	5.828	3.705	23.076
16	G328.8074 + 00.6324	5.128	3.225	23.511
17	G330.9288 − 00.4070	3.371	2.816	22.894
18	G332.2944 − 00.0962	4.303	3.150	23.133
19	G332.9868 − 00.4871	–	–	–
20	G333.0058 + 00.7707	4.460	3.653	23.331
21	G333.0682 − 00.4461	–	–	–
22	G333.1075 − 00.5020	4.601	3.251	22.557
23	G336.3684 − 00.0033	4.794	3.736	23.072
24	G338.9196 + 00.5495	4.963	3.975	23.571
25	G338.9377 − 00.4890	3.475	2.863	22.668
26	G339.5836 − 00.1265	3.441	2.829	23.016
27	G339.9267 − 00.0837	3.605	3.064	22.900
28	G340.7455 − 01.0021	3.770	2.848	22.822
29	G341.2182 − 00.2136	4.030	2.775	22.933
30	G342.7057 + 00.1260	4.440	3.369	23.112
31	G343.5024 − 00.0145	4.466	3.050	23.016
32	G343.9033 − 00.6713	3.132	2.707	22.556
33	G344.4257 + 00.0451	5.389	3.619	22.857
34	G345.5043 + 00.3480	–	–	–

H_2O masers are excellent tracers of shocked gas often associated with molecular outflows from protostellar objects. They are known to occur in all regions of star formation (Claussen et al. 1996; Forster & Caswell 1999), within both high-mass and low-mass environments. While the majority of the currently known H_2O masers are associated with star-forming regions, they can also be found in other environments, including evolved stars (Dickinson 1976) and planetary nebulae (Miranda et al. 2001). H_2O masers are present in 11 of our fields: this constitutes 52 per cent of the 21 fields that are covered by HOPS.

2.2 EXTRACTED PROPERTIES

Distances have been determined for all of the fields either by Urquhart et al. (2014b) or from the Reid et al. (2016) Bayesian model (see discussion presented in Section 4.2.1).

Due to the large uncertainties in the derived column densities, we have used the dust clump masses derived from the ATLASGAL survey (Urquhart et al. 2018) in our analysis. These values are naturally higher than expected for the NH_3 emission itself as the thermal dust emission encompasses a larger area. It is assumed, when using these values, that the densities of the regions are sufficiently high that the gas and dust are well-coupled and in local thermodynamic equilibrium.

Values for both the mass and luminosity for each region have been taken from the ATLASGAL compact-source catalogue (Urquhart et al. 2018), and are used to give a global overview of the regions. While the NH_3 emission can be used to derive parameters for individual clumps, the dust emission values are representative of the entire regions and surrounding environmental material. Bolometric luminosities for the sample range from ∼1300 to ∼670 000 $L_\odot$ and masses range from ∼330 to ∼9500 $M_\odot$.

There is no associated value for either mass or luminosity for five of our fields from the ATLASGAL survey, as these regions either lay outside the survey's coverage or are not detected in the ATLASGAL CSC.

2.2.1 Uncertainties in extracted parameters

The distances that have been assigned to each field are kinematic and so have an associated uncertainty of ±1 kpc. This uncertainty is mainly caused by peculiar motions of the clouds through the spiral arms of the Galaxy, which causes them to deviate from the rotation models. These are commonly referred to as 'streaming motions' and can lead to perturbation from the expected radial velocities of ±7 km s^{-1} (Reid et al. 2009).

The ATLASGAL dust masses are estimated to be correct to within a factor of 2–3: this is mainly due to the fact that many of the parameters involved in the calculation are poorly constrained, such as the dust-to-gas ratio and the dust absorption coefficient (Urquhart et al. 2013a). Two other parameters additionally affect the mass uncertainty: the kinetic or dust temperatures as derived from the spectral line analysis, with an approximate error of ±1.5 K, and the uncertainty in the distance measurements as mentioned in the previous paragraph.

The main source of uncertainty for the luminosity values arises from the distance uncertainties and bolometric flux calculations which results from the fitting of the spectral energy distributions for each region: these are estimated to be no more than a factor of two.

While the uncertainties may be large for the absolute values for these parameters, the whole sample is uniformly affected and so the properties should provide statistically robust results.

3 OBSERVATIONAL DATA

3.1 ATCA observations and data reduction

Observations were made of the NH_3 (1, 1) and (2, 2) inversion transitions towards 34 RMS identified MYSOs and H II regions (see Table 2 for details of observed fields). These observations were made between 2011 February 15 and 22 (Project Id: C2369; Urquhart et al. 2010). These observations were conducted using the Australia Telescope National Facilities' (ATNF) Australia Telescope Compact Array (ATCA).[1] The ATCA comprises of six 22 m diameter antennas, with five lying on a 3 km long east–west track with the sixth antenna being in a fixed position 3 km west of the track.

The array was set up in an east–west 352 configuration, utilizing five of the antennae in a compact configuration with shortest and longest baselines of 31 and 352 m, respectively. The sixth antenna was not used for this study due to the large gap in *uv*-coverage. The observations were made with the Australia Telescope Compact

[1]The Australia Telescope Compact Array is part of the Australia Telescope National Facility, which is funded by the Commonwealth of Australia for operation as a National Facility managed by CSIRO.

Table 2. Observed field parameters. Distances appended with ⋆ identify values obtained using a Bayesian distance estimator described in Reid et al. (2016).

Field id	Field name	RA (J2000)	Dec (J2000)	Number of clumps	v_{lsr} (km s^{-1})	Distance (kpc)	r.m.s noise (Jy beam^{-1})	Beam$_{maj}$ (arcsec)	Beam$_{min}$ (arcsec)
1	G261.6429 − 02.0922	08^{h}32^{m}07.46^s	−43^{d}13^{m}48.70^s	1	14.5	2.0	0.25	9.36	5.57
2	G286.2086 + 00.1694	10^{h}38^{m}32.70^s	−58^{d}19^{m}14.30^s	2	−21.1	3.0	0.30	10.28	4.94
3	G305.2017 + 00.2072	13^{h}11^{m}10.45^s	−62^{d}34^{m}38.60^s	1	−42.4	3.8	0.45	6.74	5.97
4	G309.4230 − 00.6208	13^{h}48^{m}38.86^s	−62^{d}46^{m}09.50^s	1	−42.4	3.5	0.38	7.66	5.40
5	G312.5963 + 00.0479	14^{h}13^{m}14.12^s	−61^{d}16^{m}48.90^s	1	−63.7	6.0	0.32	8.70	5.07
6	G314.3197 + 00.1125	14^{h}26^{m}26.28^s	−60^{d}38^{m}31.50^s	2	−47.5	4.2	0.33	7.61	5.47
7	G318.9480 − 00.1969	15^{h}00^{m}55.10^s	−58^{d}59^{m}06.00^s	1	−34.4	2.1	0.41	6.88	5.83
8	G322.1729 + 00.6442	15^{h}18^{m}38.29^s	−56^{d}37^{m}30.90^s	1	−57.7	3.3	0.49	7.90	5.34
9	G323.4584 − 00.0787	15^{h}29^{m}19.36^s	−56^{d}31^{m}21.70^s	1	−66.8	4.0	0.29	7.72	6.19
10	G326.4755 + 00.6947	15^{h}43^{m}18.94^s	−54^{d}07^{m}35.40^s	1	−41.2	1.8	0.58	8.78	5.77
11	G326.7249 + 00.6159	15^{h}44^{m}59.39^s	−54^{d}02^{m}19.60^s	2	−41.7	1.8	0.33	8.95	5.74
12	G327.3941 + 00.1970	15^{h}50^{m}20.07^s	−53^{d}57^{m}07.10^s	1	−89.3	5.2	0.39	9.08	5.62
13	G327.4014 + 00.4454	15^{h}49^{m}19.36^s	−53^{d}45^{m}14.40^s	1	−78.4	5.0	0.52	8.80	5.66
14	G328.2523 − 00.5320	15^{h}57^{m}59.82^s	−53^{d}58^{m}00.40^s	3	−45.1	2.7	0.44	8.08	6.01
15	G328.3067 + 00.4308	15^{h}54^{m}06.34^s	−53^{d}11^{m}39.20^s	1	−93.2	5.8	0.33	8.44	5.93
16	G328.8074 + 00.6324	15^{h}55^{m}48.36^s	−52^{d}43^{m}06.80^s	2	−41.7	2.7	0.52	9.30	5.55
17	G330.9288 − 00.4070	16^{h}10^{m}45.07^s	−52^{d}05^{m}50.20^s	1	−41.2	2.6	0.30	9.22	5.40
18	G332.2944 − 00.0962	16^{h}15^{m}45.86^s	−50^{d}56^{m}02.40^s	1	−48.9	3.1	0.33	9.52	5.47
19	G332.9868 − 00.4871	16^{h}20^{m}37.81^s	−50^{d}43^{m}49.60^s	1	−52.8	3.6	0.42	9.66	5.44
20	G333.0058 + 00.7707	16^{h}15^{m}13.79^s	−49^{d}48^{m}52.00^s	1	−49.2	3.0	0.62	9.71	5.62
21	G333.0682 − 00.4461	16^{h}20^{m}48.95^s	−50^{d}38^{m}40.30^s	1	−53.3	3.6	0.59	9.37	5.50
22	G333.1075 − 00.5020	16^{h}21^{m}14.22^s	−50^{d}39^{m}12.60^s	2	−56.5	3.6	0.38	10.10	5.27
23	G336.3684 − 00.0033	16^{h}32^{m}56.46^s	−47^{d}57^{m}52.30^s	1	−126.7	6.7	0.54	10.48	5.74
24	G338.9196 + 00.5495	16^{h}40^{m}34.04^s	−45^{d}42^{m}07.90^s	1	−62.8	4.2	1.21	9.91	5.67
25	G338.9377 − 00.4890	16^{h}45^{m}08.80^s	−46^{d}22^{m}17.00^s	2	−36.6	2.9	0.36	10.08	5.64
26	G339.5836 − 00.1265	16^{h}45^{m}58.48^s	−45^{d}38^{m}41.40^s	1	−34.3	2.6	0.37	9.75	5.28
27	G339.9267 − 00.0837	16^{h}47^{m}03.94^s	−45^{d}21^{m}20.50^s	1	−52.8	3.6	0.34	9.90	5.56
28	G340.7455 − 01.0021	16^{h}54^{m}04.05^s	−45^{d}18^{m}50.00^s	1	−29.1	2.4	0.36	10.08	5.71
29	G341.2182 − 00.2136	16^{h}52^{m}17.93^s	−44^{d}26^{m}53.00^s	1	−42.9	3.3	0.50	9.84	5.45
30	G342.7057 + 00.1260	16^{h}56^{m}02.91^s	−43^{d}04^{m}43.90^s	1	−41.0	3.4	0.46	10.05	5.50
31	G343.5024 − 00.0145	16^{h}59^{m}20.90^s	−42^{d}32^{m}38.40^s	2	−27.9	2.6	0.45	10.20	5.57
32	G343.9033 − 00.6713	17^{h}03^{m}30.11^s	−42^{d}37^{m}48.60^s	1	−29.4	2.2	0.36	10.69	6.04
33	G344.4257 + 00.0451	17^{h}02^{m}09.35^s	−41^{d}46^{m}44.30^s	2	−66.6	4.9	0.45	10.61	5.35
34	G345.5043 + 00.3480	17^{h}04^{m}22.87^s	−40^{d}44^{m}23.50^s	1	−17.7	2.4	0.66	13.27	4.81

Array Broad-band Backend (CABB; see Wilson et al. 2011 for details).

This provides a primary beam size of ∼2 arcmin [full width at half-maximum (FWHM) field of view] and a synthesized beam of 5–10 arcsec (FWHM resolution of the observations). We used a 64 MHz spectral window covering 23.6945–23.7226 GHz so as to include the NH_3 (1, 1) and (2, 2) transition in the same bandpass. Each source was observed for approximately 60 min, providing a velocity resolution of 0.4 km s^{-1} channel^{-1} and a sensitivity of 2.3 K channel^{-1} beam^{-1}.

We observed 1934−638 and 1253−055 once per day for absolute flux and bandpass calibration. The target sources were separated into groups of ∼8 closely located sources to allow the sharing of phase calibrators and minimize observing overheads. An appropriate phase calibrator was selected for each group and the observations of the target sources were sandwiched in between observations of the phase calibrator. These observation blocks arranged to be less than an hour to allow the phase calibrators to be observed at regular intervals (typically 2–3 min every hour) throughout the observing session. These allow us to correct for fluctuations in the phase and amplitude of the data caused by atmospheric and instrumental effects throughout the observations.

The calibration and reduction of these data were performed using the MIRIAD reduction package (Sault, Teuben & Wright 1995) following standard ATCA procedures. We initially imaged a region twice the size of the primary beam, choosing a pixel size to provide ∼10 pixels across the synthesized beam (1 arcsec pixels). We imaged a velocity range of 120 km s^{-1} centred on the systemic velocity of the RMS source using the native velocity resolution of the spectrometer. This resulted in spectral line cubes of 256 arcsec × 256 arcsec × 300 km s^{-1} for each transition.

These cubes were deconvolved using a robust weighting of 0.5 using a couple of hundred cleaning components per velocity channel, or until the first negative component was encountered. Weighting values less than −2 correspond to minimizing sidelobe levels only (uniform weighting), whereas values greater than +2 minimize noise levels (natural weighting). A value of 0.5 gives nearly the same sensitivity as natural weighting, but with a significantly better beam. These cubes were inspected to identify bright ammonia peaks in the field, and when detected in a map, these were integrated along the velocity axis in order to produce a high signal-to-noise ratio (SNR) map of the ammonia emission. These maps allow the peak position of the emission (taken to be the centre of the clump) and morphology of the dense gas traced by the ammonia emission to be discerned and spatially compared with the position of their embedded MYSOs and/or H II regions.

The largest well-imaged structure possible at this frequency from these snapshot observations is limited to approximately 1 arcmin due to the limited *uv*-coverage and integration time. However, many of our maps displayed evidence of large-scale emission, which,

when undersampled, can distort the processed images and lead to prominent imaging artefacts and confusion in the processed maps. This can reduce the SNR in the maps and over-resolve large-scale extended emission, breaking it up into irregular and/or multiple-component structures.

4 METHODS AND SOURCE IDENTIFICATION

4.1 Source extraction

For each source we have created NH_3 (1, 1) and (2, 2) emission intensity maps by integrating the velocity channels between $\pm 25\,\mathrm{km\,s^{-1}}$ of the peak above a 3σ threshold. These maps reveal the presence of high SNR clumps.

The `FellWalker` algorithm (Berry 2015; Moore et al. 2015) has been applied to the NH_3 (1, 1) integrated emission maps due to their higher SNR since these are more likely to trace the full extent of individual NH_3 clumps and their associated emission peaks. We have chosen to use the `FellWalker` algorithm as it has been widely used in recent studies (Paper I; Eden et al. 2017), and is robust against a wide choice of input parameters. It was required that all clumps be above a detection threshold of 3σ, where in this case σ refers to the image r.m.s. level as determined from emission-free regions of the maps. We also required that clumps be larger than the beam size ($\sim$10 pixels) in order to avoid spurious detections. Detections towards the edges of the fields were also excluded due to lower SNRs, and because source parameters are likely to be poorly constrained; this did not prove to be a significant constraint, however, as emission is generally concentrated towards the centre of the fields. There appear to be ten fields which contain imaging artefacts that resulted from the poor sensitivity of the interferometric snapshot to large-scale extended emission (as mentioned in Section 3.1). This has been mitigated through the two thresholds required for a detected clump described above. An example integrated emission map is shown in Fig. 2.

In total, `FellWalker` has identified 44 clumps in the 34 fields observed. The number of clumps detected in each field is given in Column 5 of Table 2. The clump parameters determined by `FellWalker` are given in Table 3. The clump names are derived from the coordinates of the centre of the clump which can be found in Columns 3 and 4 of this table. A total of nine fields contain more than a single clump, with the maximum number of three clumps per field. Clumps lying within the same field have coherent velocities ($\delta v < 5\,\mathrm{km\,s^{-1}}$), consistent with the hypothesis that they are all associated with the same giant molecular cloud, and many appear to be a part of the same mid-infrared structure within individual fields. In Fig. 1 we present a few examples of the NH_3 (1, 1) inversion emission contours overlaid on 8 μm IRAC images of the same region along with the associated velocity maps.

The `FellWalker` algorithm also fits the semimajor and semiminor axes of each clump, the ratio of which is used to find the corresponding aspect ratio: these are given in Columns 5–7 of Table 3. Almost every clump is extended with respect to the beam and is typically elongated: the mean and standard deviation values of the aspect ratio are 1.66 and 0.58, respectively. A histogram of the aspect ratios for the entire sample is shown in Fig.3. One clump has an aspect ratio of 4.68 (G344.4279 + 0.0514). This particular source seems to be filamentary in nature as shown in Fig. 4. Due to the low aspect ratios, any projection elements are unlikely to impact on the morphologies of the NH_3 clumps.

The angular radius for each clump has been estimated from the geometric mean of the deconvolved major and minor axis of the NH_3 emission, multiplied by a factor η that relates the r.m.s. size of the emission distribution of the source to its angular radius (equation 6 of Rosolowsky et al. 2010):

$$\theta_{\mathrm{R}} = \eta \left[\left(\sigma^2_{\mathrm{maj}} - \sigma^2_{\mathrm{bm}}\right)\left(\sigma^2_{\mathrm{min}} - \sigma^2_{\mathrm{bm}}\right) \right]^{\frac{1}{4}}, \quad (1)$$

where σ_{bm} is the r.m.s. size of the beam (i.e. $\sigma_{\mathrm{bm}} = \frac{\theta_{\mathrm{FWHM}}}{\sqrt{8ln2}}$). The value of η is taken to be 2.4 following Rosolowsky et al. (2010). An angular size has been obtained for 31 out of the 44 clumps (70 per cent): the remaining ten clumps have one axis smaller than the beam size and so a size cannot be accurately determined. This is an artefact of the detection threshold of the `FellWalker` algorithm; only NH_3 emission above this threshold is used for this analysis, although the NH_3 emission may be extended at levels below this threshold. This can result in the measured source sizes underestimating the size of the clumps and can result in sizes that are smaller than the beam (Rosolowsky et al. 2010). The obtained angular radius values range from 2.8 to 19.4 arcsec with a mean of 9.5 arcsec.

With the exception of one field not included in the ATLASGAL survey coverage (G261.6429 − 02.0922), all detected clumps in every field are enveloped by the thermal dust emission of the region, meaning that 43 of the 44 of the NH_3 clumps are associated with 32 dust sources. For the 32 ATLASGAL sources, 24 (75 per cent) are associated with a single NH_3 clump, 6 (19 per cent) with two NH_3 clumps, and 2 (6 per cent) with three NH_3 clumps. The association of multiple ammonia clumps with a single dust clump, and the fact that ammonia is tracing high volume densities allows us to investigate the substructure of these regions.

4.2 RMS and maser associations

Each detected clump has been matched with a source from the RMS survey. RMS sources that lie towards the centre of the NH_3 (1, 1) emission are classified as 'embedded', while sources located further are classified as 'associated'. Every clump has at least one associated source due to the targeted nature of the observations. There are a total 48 RMS sources in the sample, and we find that there are only 20 RMS sources (49 per cent) classified as either MYSO (15 sources) or H II region (five sources) embedded with the clumps identified in our 34 fields.

There are therefore 14 MYSOs and 14 H II regions which are not embedded. The offsets between the RMS sources and each clump's peak position can be found in Table 4, and a histogram plot of angular offsets is shown in Fig. 5. The angular offset between the position of the targeted RMS sources and the centre of the NH_3 emission for each clump ranges between 0.04 and 79.5 arcsec with a mean offset of 18.19 arcsec. The maximum offset between the source and the NH_3 emission for deeply embedded RMS sources is 21 arcsec. These values are similar to those reported in previous studies (e.g. Paper I).

4.2.1 Distances and clump radii

Distances to the RMS sources in each field have been taken from Urquhart et al. (2014b), with only two fields (G261.6429 − 02.0922 and G286.2086 + 00.1694) having no reliable distance value. We use the Reid et al. (2016) model to estimate the distances for these two sources. This method uses a Bayesian approach to assign sources to a particular spiral arm based on their (l, b, v) coordinates while taking into account kinematic distances, displacement from

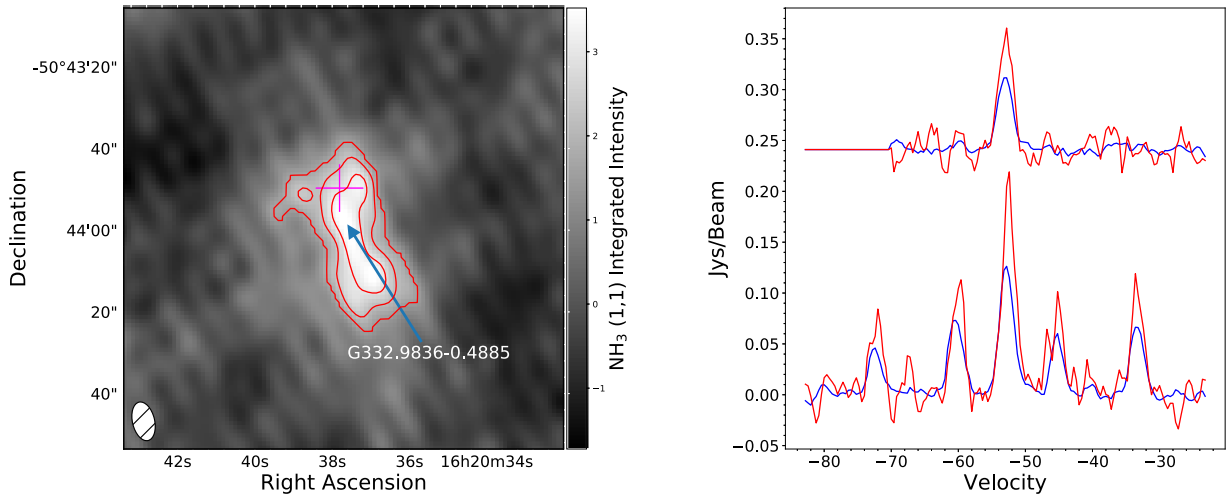

Figure 2. The left-hand panel presents an example region of an integrated NH_3 (1, 1) emission map. The central RMS source (MYSO) is marked with a magenta cross. NH_3 contours are shown in red, starting at a 3σ threshold and increasing in steps of 0.5σ, equivalent to those in Fig. 1. The right-hand panel presents associated NH_3 (1, 1) and (2, 2) spectra for this region, the average spectrum across the emission above the 3σ threshold is shown in blue, while the spectrum from the peak integrated position is shown in red.

Table 3. `FellWalker` source catalogue for detected clumps. All parameters that have been derived in the table have been obtained using the NH_3 emission maps. Columns: (1) field identification number; (2) clump name derived from Galactic coordinates of the peak emission of the source; (3)–(4) right ascension and declination of source in J2000 coordinates; (5)–(6) semimajor and semiminor axis of clumps; (7) aspect ratio (σ_{maj} / σ_{min}); (8) radius for each clump; (9)–(10) sum and peak emission values; (11) signal-to-noise ratio.

Field id (1)	Clump name (2)	RA (J2000) (3)	Dec. (J2000) (4)	σ_{maj} (arcsec) (5)	σ_{min} (arcsec) (6)	Aspect Ratio (7)	Radius (pc) (8)	Sum (K km s^{-1}) (9)	Peak (K km s^{-1}) (10)	SNR (11)
1	G261.6454 − 2.0884	$08^h32^m09.00^s$	$-43^d13^m47.57^s$	5.43	3.75	1.45	0.07	409.24	1.90	7.21
2	G286.2124 + 0.1697	$10^h38^m34.18^s$	$-58^d19^m17.65^s$	4.13	2.62	1.57	–	370.88	2.96	9.06
2	G286.2052 + 0.1706	$10^h38^m31.49^s$	$-58^d19^m01.99^s$	3.27	1.86	1.76	–	137.05	2.16	6.24
3	G305.2084 + 0.2061	$13^h11^m13.80^s$	$-62^d34^m41.23^s$	4.65	3.87	1.20	0.14	1423.72	10.29	22.03
4	G309.4208 − 0.6204	$13^h48^m37.80^s$	$-62^d46^m09.98^s$	7.45	6.57	1.13	0.26	950.19	2.58	6.63
5	G312.5987 + 0.0449	$14^h13^m15.38^s$	$-61^d16^m54.37^s$	3.64	2.25	1.62	–	231.04	2.33	6.53
6	G314.3214 + 0.1146	$14^h26^m26.47^s$	$-60^d38^m20.51^s$	4.31	3.37	1.28	0.12	262.18	2.11	6.18
6	G314.3197 + 0.1092	$14^h26^m26.64^s$	$-60^d38^m40.85^s$	2.33	1.45	1.61	0.09	53.54	1.64	4.08
7	G318.9477 − 0.1959	$15^h00^m55.30^s$	$-58^d58^m52.14^s$	5.94	4.99	1.19	0.12	1298.33	5.00	11.97
8	G322.1584 + 0.6361	$15^h18^m34.63^s$	$-56^d38^m24.79^s$	6.50	3.79	1.72	0.15	1096.10	5.67	11.18

Note: Only a small portion of the data is provided here, the full table is only available in electronic format.

the Galactic plane, and proximity to individual parallax sources. We find the distance to G261.6429 − 02.0922 to be 2.02 ± 0.78 kpc and 3.0 ± 1.23 kpc for G286.2086 + 00.1694. This additional information gives a complete list of distances for every observed field; these are given in the last column of Table 1. Overall, the fields have a minimum and maximum distance of 1.80 and 6.70 kpc, respectively, with a mean distance of 3.46 ± 1.22 kpc. We find no difference between the distances towards MYSOs or H II regions. As mentioned in the previous section we have calculated the angular radius for 31 out of the 44 (70 per cent) detected clumps, and with the determined distances, it is possible to calculated the physical clump size. We find that the clumps have a mean radius of 0.15 pc with a range between 0.04 and 0.36 pc (see Table 3), which is on the size scale of individual cores or small stellar systems.

4.2.2 Image analysis and classification

The GLIMPSE three-colour images provide a view into the infrared properties of the environments, and can be used to detect multiple phenomena as discussed in Section 2.0.1. We present three-colour IRAC images of the observed regions in Figs. 6–7(GLIMPSE images for all regions can be found in the appendix), and have overplotted contours of the ammonia and dust emission in order to examine the morphological correlation of molecular gas and mid-infrared emission and the embedded star formation.

We have constructed a classification system based on the morphologies of the NH_3 emission and how it relates to the RMS sources and thermal dust emission from an inspection of these composite images. Fields which contain a single well-defined clump that is well-correlated with the ATLASGAL emission and which have an RMS source located centrally towards the NH_3 emission are classified as *early star forming* (ESF). Fields that show a more unstructured and broken morphology, generally containing multiple NH_3 clumps and RMS sources that are not coincident with an NH_3 clump are classified as *late star forming* (LSF), as it is expected that the feedback from forming massive star has a significant disruptive impact on its surroundings. All regions show signs of ongoing star formation processes, and Figs 6 and 7 show some examples of regions that are classified as ESF and LSF, respectively.

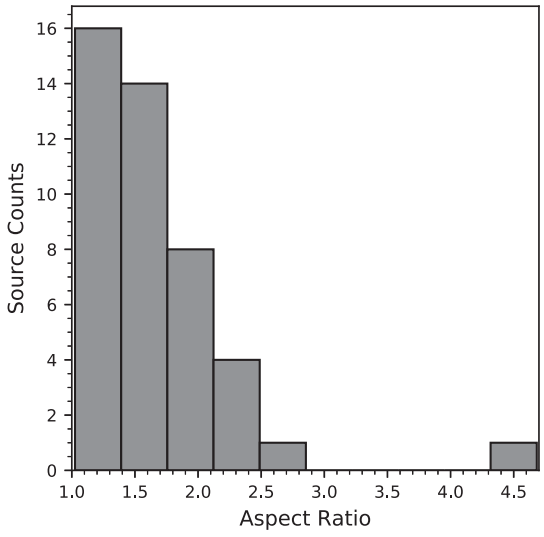

Figure 3. Histogram presenting the aspect ratios for all detected clumps (i.e. σ_{maj} / σ_{min}).

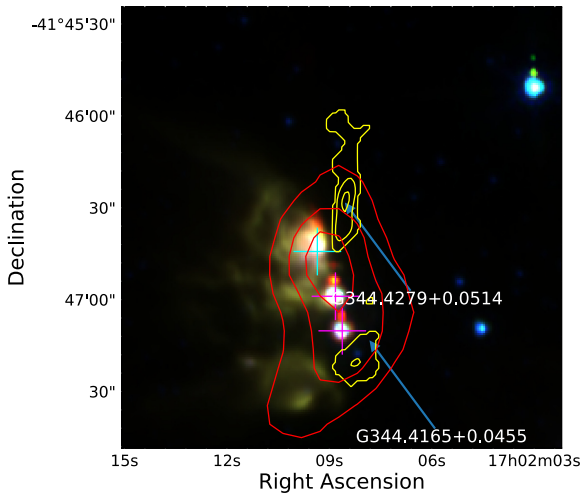

Figure 4. Example RGB GLIMPSE image of region (G344.4257 + 00.0451), overlaid with NH_3 and ATLASGAL contours in yellow and red, respectively, the contours levels are equivalent to those in Fig. 1. This field contains two clumps, one of which (G344.4279 + 0.0514) presents the most elongated structure in the sample, with a filamentary morphology.

Three of the fields in this sample were classified as 'quiescent' as they shown no signs of current star formation. These quiescent clumps are well aligned with the dust emission in the area but show no signs of having undergone any star formation (i.e. no evidence of an embedded mid-infrared point source, which is usually taken as evidence of the presence of a proton ongoing stellar object). While all observations were targeted towards RMS sources, the offset between the NH_3 emission and the nearest RMS object for these three regions is sufficiently large to conclude that they are not associated. An example of a quiescent clump is shown in the left panel of Fig. 1 (G326.7270 + 0.6228).

If a field contains both an embedded MYSO and an H II region (or multiple of either), then the most centrally located source is taken as the primary association (10 fields, 6 of which are ESF and 4 are LSF). There are 15 fields in the sample that have been classified as ESF fields. Of these 15, 13 are associated with MYSOs (as defined by the RMS survey), with the remaining two associated with an H II region. Sixteen fields have been classified as LSF. Only six of these fields contain an embedded MYSO, while the majority of fields are associated with an HII region. An inspection of the images indicates that the majority of early star-forming regions are associated with MYSOs (87 per cent), while later regions are dominated by H II regions (63 per cent). MYSOs, therefore, appear to be still very embedded, while the majority of the H II regions appear to be actively disrupting their natal clump and breaking out of their dust cocoons (as shown in Fig. 1). This is not obvious in the ATLASGAL data (which is sensitive to the whole column of gas along the line of sight, and also has lower spatial resolution than the NH_3 observations) but can clearly be seen by the NH_3 emission,

Table 4. Table of RMS associations with corresponding angular offset values for all detected clumps. All RMS names appended with ∗ relate to RMS objects deeply embedded within the NH_3 clump shown.

Field id	Clump name	RMS name	RMS type	Angular offset (arcsec)
1	G261.6454 − 2.0884	G261.6429 − 02.0922	H II region	25
2	G286.2124 + 0.1697	G286.2086 + 00.1694	YSO	22
2	G286.2052 + 0.1706	G286.2086 + 00.1694	YSO	22
3	G305.2084 + 0.2061	G305.2017 + 00.2072A	YSO	49
4	G309.4208 − 0.6204	G309.4230 − 00.6208	YSO	7
5	G312.5987 + 0.0449	G312.5963 + 00.0479	H II region	21
6	G314.3214 + 0.1146	G314.3197 + 00.1125	YSO	11
6	G314.3197 + 0.1092	G314.3197 + 00.1125	YSO	14
7	G318.9477 − 0.1959	G318.9480 − 00.1969A∗	YSO	0
8	G322.1584 + 0.6361	G322.1729 + 00.6442	YSO	79
9	G323.4537 − 0.0830	G323.4584 − 00.0787	H II region	27
10	G326.4753 + 0.7030	G326.4755 + 00.6947	YSO	43
11	G326.7270 + 0.6228	G326.7249 + 00.6159B	YSO	26
11	G326.7216 + 0.6166	G326.7249 + 00.6159A	H II region	18
12	G327.3933 + 0.1987	G327.3941 + 00.1970∗	YSO	20
13	G327.4030 + 0.4447	G327.4014 + 00.4454∗	H II region	3
14	G328.2544 − 0.5318	G328.2523 − 00.5320A∗	YSO	0
14	G328.2610 − 0.5278	G328.2523 − 00.5320A	YSO	29
14	G328.2607 − 0.5206	G328.2523 − 00.5320B	YSO	46
15	G328.3021 + 0.4377	G328.3067 + 00.4308	H II region	48
16	G328.8057 + 0.6347	G328.8074 + 00.6324	H II region	18
17	G328.8109 + 0.6336	G328.8074 + 00.6324	H II region	17
18	G330.9259 − 0.4066	G330.9288 − 00.4070∗	H II region	10
19	G332.2962 − 0.0927	G332.2944 − 00.0962	H II region	11
20	G332.9836 − 0.4885	G332.9868 − 00.4871∗	YSO	9
21	G333.0179 + 0.7654	G333.0162 + 00.7615	H II region	12
22	G333.0674 − 0.4464	G333.0682 − 00.4461∗	YSO	3
23	G333.1038 − 0.5026	G333.1075 − 00.5020	YSO	19
23	G333.1120 − 0.4996	G333.1075 − 00.5020	YSO	10
24	G336.3696 − 0.0045	G336.3684 − 00.0033A	H II region	9
25	G338.9231 + 0.5523	G338.9196 + 00.5495∗	YSO	17
25	G338.9306 − 0.4948	G338.9377 − 00.4890B∗	YSO	32
25	G338.9368 − 0.4889	G338.9377 − 00.4890B∗	YSO	5
26	G339.5845 − 0.1267	G339.5836 − 00.1265∗	YSO	15
27	G339.9257 − 0.0825	G339.9267 − 00.0837∗	YSO	10
28	G340.7460 − 1.0005	G340.7455 − 01.0021∗	YSO	14
29	G341.2166 − 0.2113	G341.2182 − 00.2136∗	YSO	1
30	G342.7069 + 0.1250	G342.7057 + 00.1260B∗	YSO	2
31	G343.5027 − 0.0133	G343.5024 − 00.0145∗	H II region	1
31	G343.5058 − 0.0172	G343.5024 − 00.0145∗	H II region	21
32	G343.9043 − 0.6705	G343.9033 − 00.6713∗	YSO	2
33	G344.4279 + 0.0514	G344.4257 + 00.0451A	H II region	20
33	G344.4165 + 0.0455	G344.4257 + 00.0451C	YSO	12
34	G345.5044 + 0.3484	G345.5043 + 00.3480∗	YSO	0

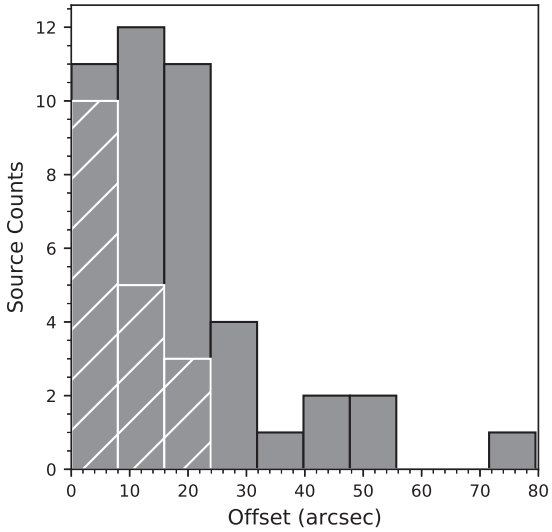

Figure 5. Histogram presenting the distribution of the angular offsets between associated RMS sources and peak clump positions, embedded sources are shown with hatched markings.

which has a critical density of $n \sim 1.8 \times 10^3\,\mathrm{cm}^{-3}$ and so only traces the high volume–density substructure within the clumps.

Our visual examination of the dust- and ammonia-overlaid three-colour IRAC maps has resulted in the identification of three visually distinct stages (quiescent, ESF, and LSF). We need to demonstrate that this sequence is reliable, and one such approach is to compare the physical properties of these different types of regions and determine whether there are any physical trends that support our visual classification.

We have used data from the MMB survey and the HOPS in order to provide more information on the regions presented in this study. Overall, we find that 52 H_2O and 31 methanol masers are associated with our 34 fields. A breakdown of this sample is presented in Table 5 for each classification and central RMS object.

GLIMPSE 8 μm images have been used to provide context for the maser distribution with NH_3 and ATLASGAL contours: two example maps of these can be found in Fig. 8. The image shown in the left-hand panel shows a region which has been defined as quiescent with an MYSO and H II region in close proximity to the west; however, there are also coincident masers (8 H_2O and 1 methanol) towards the centre of the gas and dust emission. Therefore this region is unlikely to be quiescent and is probably in an early protostellar stage of star formation, as the presence of maser emission indicates that a central core is likely to have already developed. This is the case for all three regions which have been identified as quiescent (G305.2017+00.2072, G322.1729+00.6442, and G326.4755 + 00.6947), all of which have at least one methanol maser towards the centre of the field. These quiescent fields have been reclassified as early star forming, leaving no quiescent regions in the sample. We have, therefore, classified 18 fields as being ESF and 16 fields as LSF. The right-hand panel of Fig. 8 presents another region with a relatively high number of maser detections. This field is classified as early star forming and is associated with a total of 12 masers (10 H_2O and 2 methanol). All of these are found towards the central RMS object. This source appears to be located on the edge of an evolved H II region and so this may be an example of triggered star formation (see further discussion in Section 5.4.4).

5 DETERMINATION OF PHYSICAL PROPERTIES

5.1 Ammonia line fitting

We have conducted a spectral line analysis for all 44 clumps which have been identified by `FellWalker`.

This study makes use of the method presented in Rosolowsky et al. (2008) for estimating physical parameters from ammonia spectra, using a non-linear least-squares minimization code to determine the optimal fit to the observed spectra. This technique simultaneously fits observed the NH_3 inversion transitions [in our case, the (1, 1) and (2, 2) transitions] using the physical parameters (such as kinetic temperature and optical depth) as fitting parameters. This avoids potential systematic errors that may be encountered when transitions are fitted independently, and automatically determines uncertainties for the physical parameters of the system. We use `pyspeckit` (Ginsburg & Mirocha 2011), a PYTHON implementation of this method to fit the 18 individual (1, 1) and 21 (2, 2) hyperfine transitions simultaneously, determining the free parameters which include the kinetic (T_{kin}) and excitation (T_{ex}) temperatures, FWHM line width (Δv), radial velocity (v_{LSR}), and the NH_3 column density. While the satellite lines of the (2, 2) emission are generally undetected in our observations, a well-detected (2, 2) main line sufficiently constrains the solution, allowing good determination of the free parameters.

This model assumes that the kinetic temperature is less than $T_0 = 41.5\,\mathrm{K}$, which is the energy difference associated with these lowest two inversion transitions, implying that only these first two energy states are significantly populated. The reduced data cubes are ∼4.3 arcmin in diameter and gridded using 1 arcsec pixels with contours levels starting at 3σ and increasing in levels of 0.5σ.

For each of the data cubes, a pixel-by-pixel line analysis has been performed in order to extract spectra which can then be fit using the aforementioned technique. The moment maps of the ammonia spectra were used to provide initial guesses at the velocity and line-width parameters, which were then refined by a pixel-by-pixel fitting process. Only pixels above a 3σ threshold were fitted to avoid contamination of the results due to the inclusion of pixels with low SNRs. The observed maps have been spatially smoothed to twice the size of the original beam (∼20 arcsec) in order to improve the SNR of individual spectra. Example NH_3 spectra are shown in Fig. 2. and the derived peak and median values for the fitted parameters for all of the clumps are given in Table 6.

5.1.1 *Thermal and non-thermal line widths*

The observed FWHM line width (Δv_{obs}, a free parameter determined by the fitting procedure) is a convolution of the intrinsic line width of the source (Δv_{int}) and the velocity resolution of the observations. We remove the $0.4\,\mathrm{km\,s^{-1}}$ spectrometer channel width by subtracting this value from the measured FWHM line width in quadrature:

$$\Delta v_{\mathrm{int}} = \sqrt{\left(\Delta v_{\mathrm{obs}}^2 - (0.4)^2\right)}. \quad (2)$$

The peak intrinsic line widths have mean and median values of 3.85 ± 0.3 and $3.28\,\mathrm{km\,s^{-1}}$, respectively. These values are similar to values found in previous studies (Sridharan et al. 2002; Wienen et al. 2012).

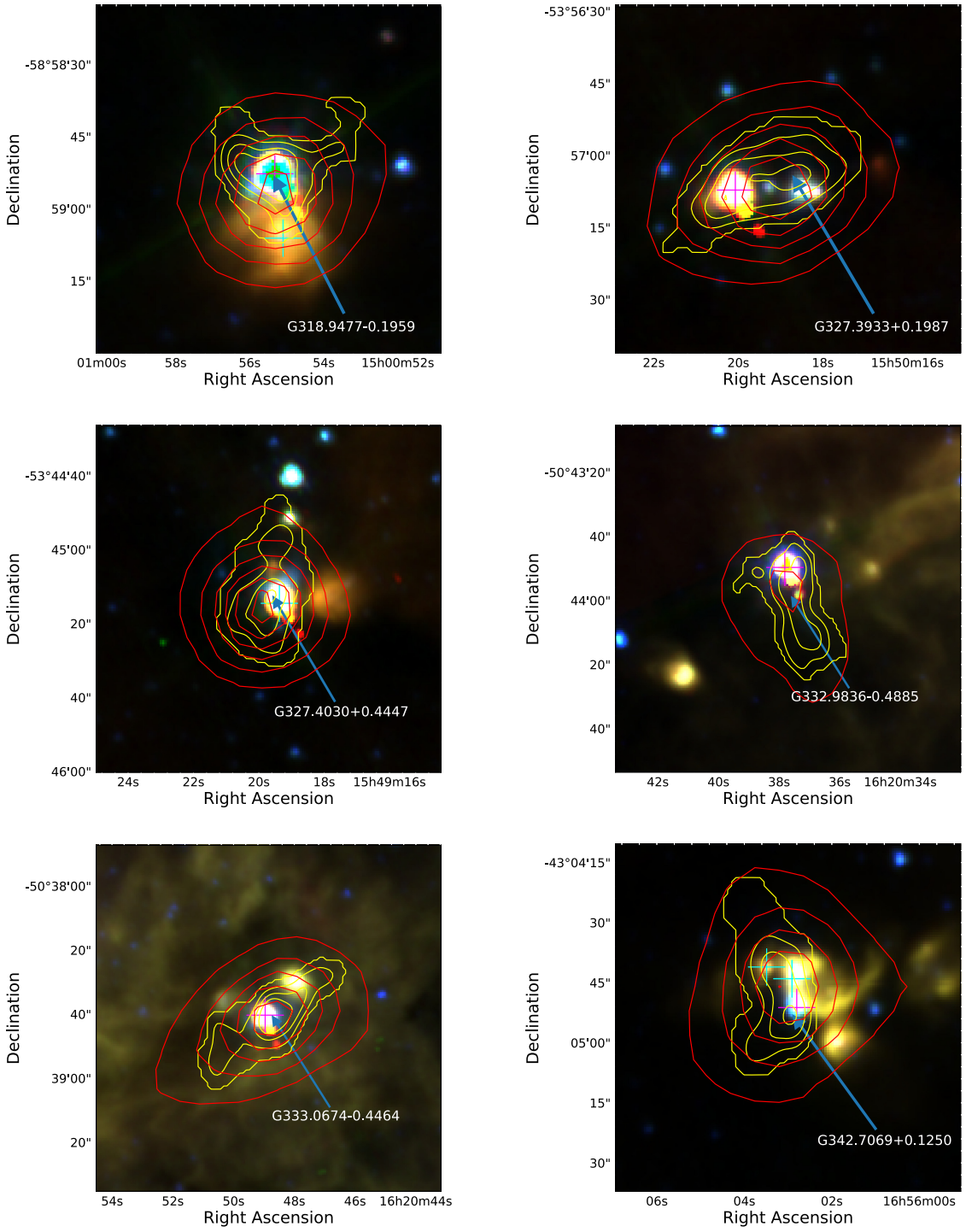

Figure 6. Example maps of early star-forming regions, presented in each panel is a three-colour GLIMPSE image overlaid with NH_3 emission and ATLASGAL dust emission contours in yellow and red, respectively, the contours levels are equivalent to those in Fig. 1. The wavelengths for the RGB channels are 8, 4.5, and 3.4 μm, respectively. MYSOs and H II regions identified by the RMS survey are shown with magenta and cyan crosses, respectively. Clump positions and names are shown with blue arrows and white labels. GLIMPSE images for the remaining 12 ESF fields can be found in the appendix.

The line widths of the ammonia spectra consist of thermal and non-thermal components, where the thermal component can be estimated using:

$$\Delta v_{\rm th} = \sqrt{\left(\frac{8\ln 2 k_{\rm B} T_{\rm kin}}{m_{\rm NH_3}}\right)}, \quad (3)$$

where 8ln2 is the conversion between the velocity dispersion σv and the FWHM line width Δv, $k_{\rm B}$ is the Boltzmann constant, and $m_{\rm NH_3}$ is the mass of an ammonia molecule (17.03 AMU). The measured line widths themselves are significantly broader than this estimation (for gas temperatures of 20 K, $\Delta v_{\rm th}$ is $\sim$0.22 km s^{-1}), meaning there is a large contribution from non-thermal components such as supersonic turbulent motions, outflows, shocks, and magnetic fields

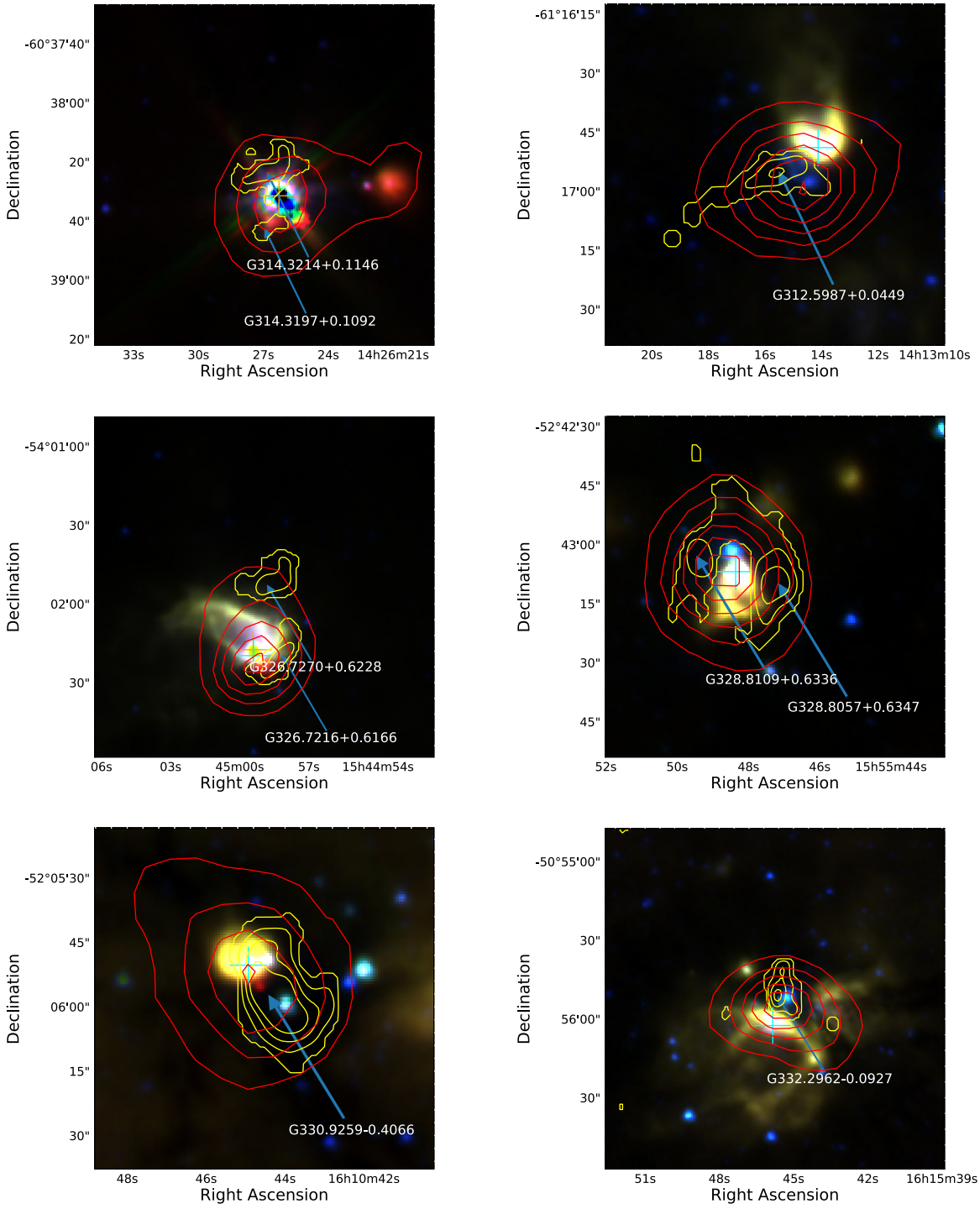

Figure 7. Image details are the same as for Fig. 6, but for a sample of late star-forming regions. GLIMPSE images for the remaining 10 LSF regions can be found in the appendix.

(Elmegreen & Scalo 2004). The impact on the data from these mechanisms can be derived by subtracting the thermal component in quadrature:

$$\Delta v_{\rm nt} = \sqrt{\left(\Delta v_{\rm int}^2 - \frac{8\ln 2 k_{\rm B} T_{\rm kin}}{m_{\rm NH_3}}\right)}. \quad (4)$$

The gas pressure ratio can be estimated from the ratio of the thermal and non-thermal line widths, which are equivalent to the thermal and non-thermal pressures within the gas:

$$R_{\rm p} = \left(\frac{\Delta v_{\rm th}^2}{\Delta v_{\rm nt}^2}\right). \quad (5)$$

These ratio values are quite low (the mean and median values of the mean pressure for each clump is 0.012 and 0.01, respectively, with a range of 0.002–0.03, see Table 7), indicating that the pressure in the gas is dominated by non-thermal motion.

Table 5. Distribution of masers across the sample.

Classification	Methanol masers	H_2O masers
ESF	20	41
LSF	11	11
YSO	23	32
H II region	8	15

5.1.2 Beam filling factor

The previously mentioned assumption of kinetic temperature limit mentioned above ($T_{\rm kin} < T_0 = 41.5$ K) provides a significant restriction on this study.

For $T_{\rm kin} < T_0$, the calculation of the rotation temperature can be completed using the following equation (Walmsley & Ungerechts 1983; Swift, Welch & Di Francesco 2005):

$$T_{\rm rot} = T_{\rm kin} \left\{ 1 + \frac{T_{\rm kin}}{T_0} \ln \left[1 + 0.6 \exp\left(-15.7 / T_{\rm kin}\right) \right] \right\}^{-1}. \quad (6)$$

We have used the calculated values of rotational temperature in order to determine the beam filling factor for the entire sample:

$$B_{\rm ff} = \frac{T_{\rm ex}}{T_{\rm rot}}. \quad (7)$$

The calculated excitation temperatures (2.77–7.10 K) and beam filling factors are relatively low (0.09–0.21 with a mean value of 0.15), which is similar to other studies (Friesen et al. 2009; Paper I; Urquhart et al. 2011). The less-than-unity values of the filling factor suggest that although the emission is extended with respect to the beam, clumps are likely to consist of a significant number of smaller dense substructures (cores), which when convolved with the beam results in the appearance of an extended emission region.

5.1.3 Column densities

The NH_3 column density is calculated as a free parameter using the inversion transition hyperfine structure. This essentially uses the derived rotation temperature, and so has already taken into account the beam filling factor. The optical depth is calculated from the ratio between the observed brightness of the main and inner satellite lines, but low SNRs for the satellite lines produce large uncertainty in this ratio, resulting in a very poorly constrained optical depth for weakly detected pixels. As the column density of the NH_3 gas is directly derived from the optical depth, the majority of column density values are also unreliable. Pixels with this feature were located based on their high relative errors (>100 per cent) from the associated column density error maps produced by the fitting routine and removed from the analysis.9

Example maps of the various parameters described in this section can be found in Fig. 9. The statistical values for each parameter are given in Table 6 and a summary of these for the whole sample is given in Table 7.

5.1.4 Uncertainties on the fitted parameters

The `FellWalker` algorithm provides no estimation of the uncertainties for the position or size of the detected clumps (which is a function of beam size and SNR); we calculate the mean error of this to be ∼3.7 arcsec (beam size / $\sqrt{\rm SNR}$).

The procedure used during the fitting process automatically computes error maps for each individual free parameter which is derived from the ammonia spectra, the uncertainties for which are the derived uncertainties from the non-linear least-squares fitting using the covariance matrix. These uncertainties include statistical and systematic errors arising from the model and also error propagation, a detailed explanation of the errors for this fitting routine can be found in (Rosolowsky et al. 2008). Uncertainties for the temperatures ($T_{\rm kin}$, $T_{\rm ex}$, $T_{\rm rot}$) and velocity are relatively small, typically less than 0.5 K and 0.1 km s^{-1}, respectively. The errors for the beam filling factor are also relativity low as the values are calculated from the ratio of the excitation and rotational temperatures. As mentioned in Section 5.1.3, errors for the majority of optical depth and column density calculations cause these values to be unreliable.

A number of fields within the sample show signs of multiple components: visual inspection indicates that five fields have at least two spectral components in either the NH_3 (1, 1) or (2, 2) transitions, as there is a clear difference between the average and peak spectra as shown in Fig. 10. The NH_3 (1, 1) average spectrum appears coherent, whereas the peak spectrum shows an indication of multiple components at different velocities, which are unresolved, as the FWHM of each NH_3 spectral line component is not separated. Multiple components tend to increase the measured line widths, and it is difficult to resolve both individual components without higher spectral and angular resolution. Affected regions can be found labelled with a star (∗) in Table 6.

The statistical values for the luminosity and mass of all dust clumps can be found in Table 7, while the values for individual sources are given in Table 1. Fitted parameter maps for all of the regions, along with the corresponding GLIMPSE images, can be found in the appendix.

6 DISCUSSION OF PHYSICAL PARAMETERS

6.1 Overview of derived properties

We have derived multiple properties from the NH_3 spectral line analysis (kinetic temperatures, FWHM line widths, beam filling factors, and pressure ratios), which have been supplemented with parameters from the ATLASGAL survey (luminosities and masses). Values for the temperatures and beam filling factors, which range between 10 and 40 K, and 0.09 and 0.21, along with our measured FWHM line widths, are similar to previous studies (Sridharan et al. 2002; Wienen et al. 2012).

6.2 Evolutionary sequence

As outlined in the introduction, the main purpose of this study is to investigate the initial physical conditions of the environments of high-mass stars in order to better understand where they form and how their feedback in turn affects their environments. We examine morphology of the molecular gas with respect to the different type of embedded objects and investigate how they are affecting their local environment. The accumulated ATLASGAL survey data has aided in the understanding of these regions and the larger structure in the local environment and how it relates to the dense gas as mapped by the NH_3 emission.

It is possible to construct a rudimentary evolutionary track by incorporating all of this information and the three types of classifications for each field. An example of how this can be visualized is shown in Fig. 11. A region begins in the quiescent/protostellar state with no observable ongoing formation and no visible embedded objects at the infrared wavelengths of the GLIMPSE survey (3.6, 4.5, and 8 μm). These initial regions are already associated

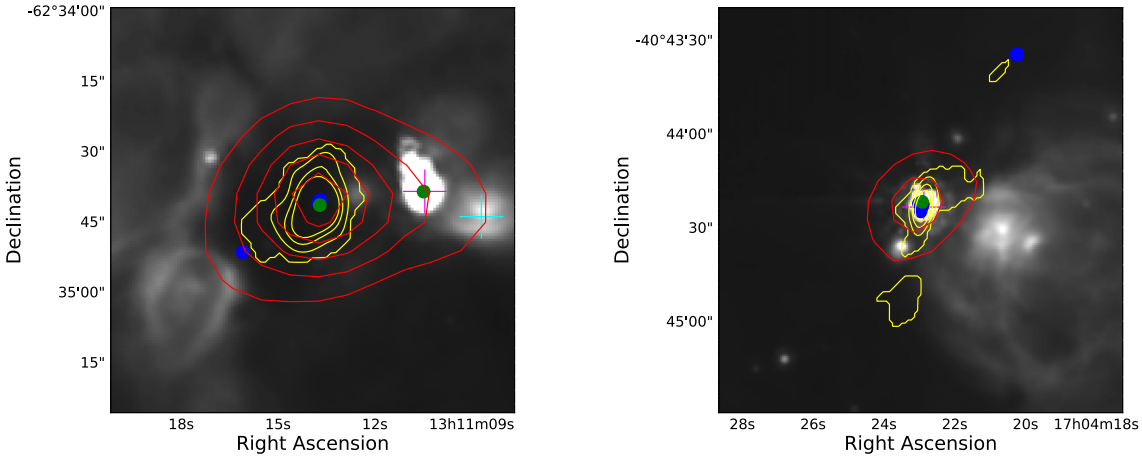

Figure 8. GLIMPSE 8 μm images showing two regions from the sample (G305.2017+00.2072 and G345.5043 + 00.3480). The red contours outline the ATLASGAL dust emission and the yellow contours outline the NH_3 emission, while the green and blue filled circles represent the methanol and H_2O maser detections, respectively, the contours levels are equivalent to those in Fig. 1. Magenta markers represent the position of identified MYSOs, while cyan markers show the positions of H II regions.

Table 6. Detected NH_3 clump parameters. The columns are as follows: (1) field ID given in Table 1; (2) name of clump derived from Galactic coordinates of peak emission of each clump; (3)–(4) radial velocity and intrinsic FWHM line width; (5)–(7) show different calculated temperatures for each clump; (8) beam filling factor (T_{ex}/T_{rot}); (10) NH_3 column density. (For each cell, initial values are peak values, with median values shown in parenthesis for the pixel by pixel fitting routine.) Regions appended with ∗ identified regions with contain dual spectra components.

Field id (1)	Clump name (2)	v_{lsr} (km s^{-1}) (3)	Δv (km s^{-1}) (4)	T_{ex} (K) (5)	T_{rot} (K) (6)	T_{kin} (K) (7)	B_{ff} (8)	log(N(NH_3)) (cm^{-2}) (9)
1	G261.6454 − 2.0884	14.55	2.97 (2.45)	3.15 (2.82)	23.89 (21.07)	28.86 (24.49)	0.15 (0.13)	16.41 (15.96)
2	G286.2124 + 0.1697	− 21.15	2.84 (1.53)	2.86 (2.83)	17.28 (16.50)	19.15 (18.12)	0.17 (0.17)	15.94 (14.79)
2	G286.2052 + 0.1706	− 18.09	2.91 (2.13)	2.94 (2.81)	23.98 (19.43)	29.00 (22.10)	0.17 (0.15)	14.70 (14.35)
3	G305.2084 + 0.2061	− 41.94	8.69 (6.50)	2.93 (2.82)	27.81 (25.20)	35.60 (31.01)	0.14 (0.11)	17.60 (15.45)
4	G309.4208 − 0.6204	− 42.51	1.66 (1.46)	2.84 (2.81)	17.88 (15.90)	19.96 (17.34)	0.22 (0.18)	18.87 (17.42)
5	G312.5987 + 0.0449	− 63.55	3.08 (2.69)	2.85 (2.82)	24.09 (20.97)	29.18 (24.34)	0.15 (0.13)	15.27 (14.74)
6	G314.3214 + 0.1146	− 47.44	1.74 (1.62)	2.81 (2.80)	18.85 (16.95)	21.29 (18.71)	0.20 (0.16)	18.78 (15.95)
6	G314.3197 + 0.1092	− 48.26	2.11 (1.85)	2.77 (2.77)	17.15 (16.31)	18.98 (17.88)	0.19 (0.17)	17.42 (17.11)
7	G318.9477 − 0.1959	− 34.54	3.98 (2.82)	2.88 (2.83)	22.26 (19.99)	26.29 (22.91)	0.17 (0.14)	18.57 (17.41)
8	G322.1584 + 0.6361	− 57.91	4.47 (3.83)	2.87 (2.81)	29.43 (23.28)	38.65 (27.87)	0.14 (0.12)	19.02 (16.69)

Note: Only a small portion of the data is provided here, the full table is only available in electronic format.

Table 7. Statistical properties for the whole sample.

Parameter	Number	Mean	Standard error	Standard deviation	Median	Min	Max
Aspect ratio	44	1.66	0.09	0.60	1.57	1.03	4.68
Angular offset	44	18.19	2.41	15.97	15.32	0.04	79.5
Distance (kpc) (fields)	34	3.46	0.21	1.22	3.30	1.80	6.70
Radius (pc) (fields)	34	0.15	0.01	0.09	0.12	0.04	0.36
T_{kin} (mean) (K)	44	22.31	0.74	4.90	21.47	14.43	36.67
FWHM line width (mean) (km s^{-1})	44	2.69	0.17	1.15	2.47	1.28	6.09
Pressure ratio (mean)	44	0.01	0.001	0.01	0.01	0.002	0.02
Beam filling factor (mean)	44	0.15	0.004	0.02	0.15	0.09	0.21
N(NH_3) (mean)	44	16.72	0.26	1.71	16.58	14.33	22.36
log(field mass) ($M_\odot$)	29	3.21	3.18	0.07	3.18	2.52	3.98
log(field luminosity) ($L_\odot$)	29	4.37	0.13	0.72	4.46	3.13	5.83

with methanol masers, and are therefore harbouring massive protostars (upper panel of Fig. 11). The morphology of these clumps is relatively unbroken with only a single clump of emission. As accretion processes drive the embedded objects into the MYSO stage, the environments increase in temperature and turbulence as the MYSOs feed back into their local environment. These early-stage clumps have high signal-to-noise and a well-defined structure with at least one RMS object embedded towards the centre of the emission (middle panel of Fig. 11). Once the MYSO has reached maturity and it begins to produce an H II region, it will disrupt

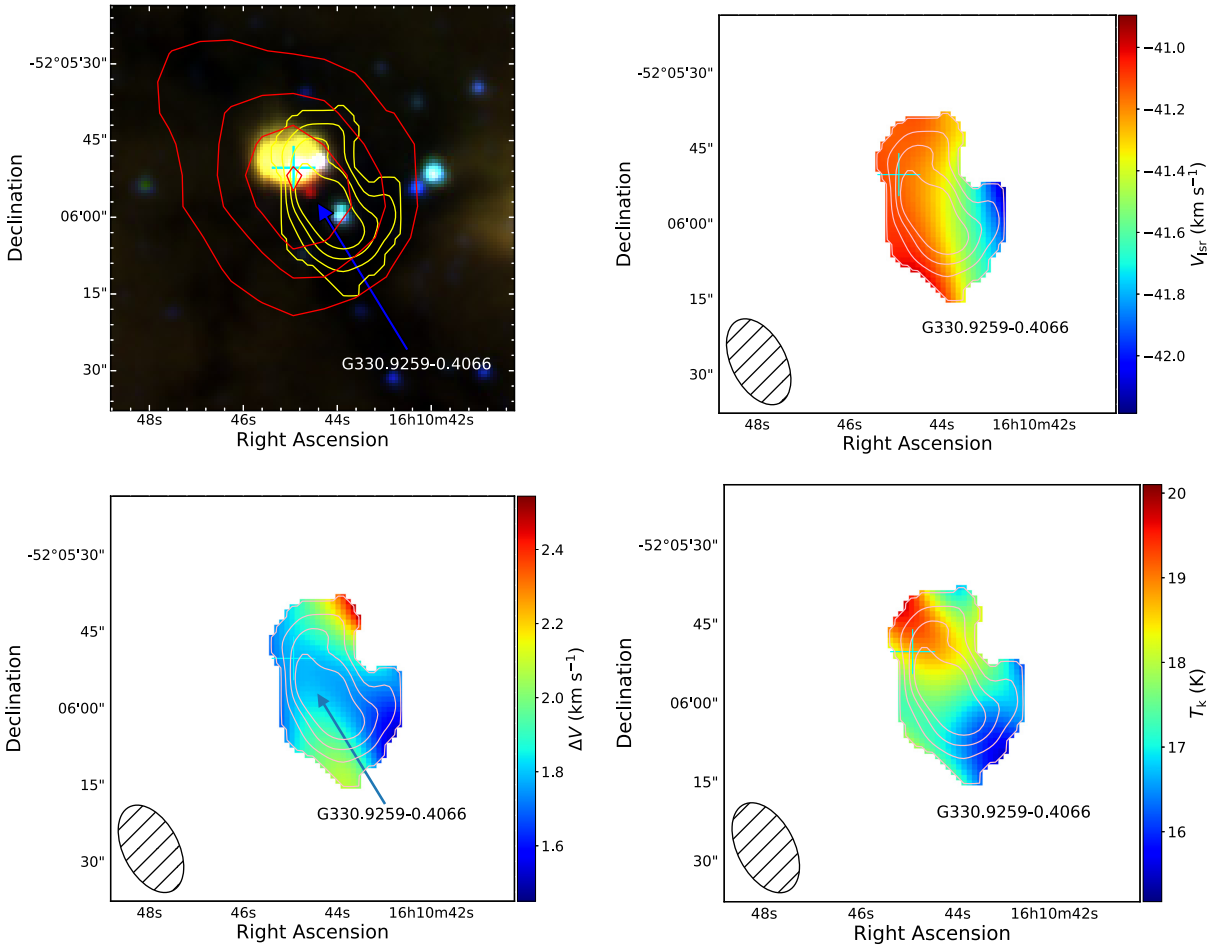

Figure 9. Sample maps of the various parameters described in Sections 4 and 5.1 for region G330.9288−00.4070. In the upper left panel we present a three-colour RGB image created from the GLIMPSE data, overplotted with the NH_3 and ATLASGAL emission in yellow and red contours respectively. The contours levels are equivalent to those in Fig. 1. From the upper right clockwise to the bottom left, the maps presented are the velocity, velocity dispersion, and the kinetic temperature. The blue arrows and black labels identify ammonia clumps identified using the `FellWalker` algorithm. Orange and cyan markers identify the positions of any MYSOs or H II regions, respectively. Beam sizes are shown as a hatched black ellipsoids in the lower right corner of each plot.

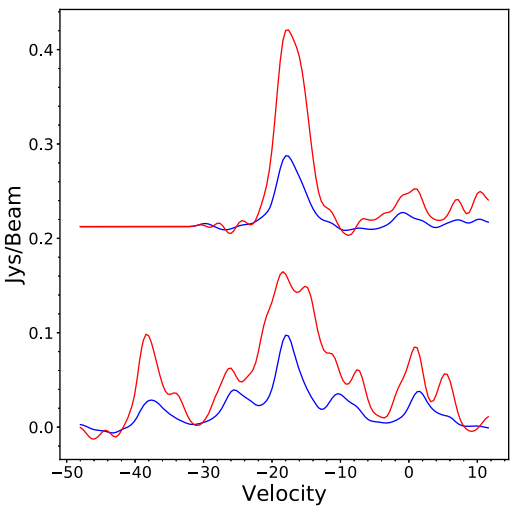

Figure 10. Example NH_3 spectra of field G345.5043 + 00.3480. The peak and average spectra across the clump are shown in red and blue, respectively. The spectra have been smoothed with a 1D Gaussian kernel ($\sigma = 2$).

its environment, fragmenting any dense material which could be observed via NH_3 emission (lower panel of Fig. 11).

This proposed sequence of events is similar in nature to previous studies (e.g. Zinnecker & Yorke 2007; Chambers et al. 2009; Battersby et al. 2014), where similar evolutionary sequences are presented using a number of different tracers. Chambers et al. (2009) proposed an evolutionary sequence for infrared dark clumps, this begins with a quiescent clump transitioning into an active clump and finally into a more evolved 'red' clump. These classifications were based solely on IR emission, 24 μm point sources and enhanced 8 μm emission. That evolutionary model is similar in nature to what is presented in this study, although the main focus for this work is on the distribution and offsets of NH_3 and 870 μm emission, relative to the positions of RMS sources. This work also gives a physical view to other large sample studies, such as (Urquhart et al. 2014c; fig. 21), which includes ATLASGAL CSC data and shows two distinct phases, accretion and dispersion, which can clearly be seen in our observations. While this may not be a robust evolutionary sequence model for massive star formation, our data do nicely highlight differences between each evolutionary stage identified here.

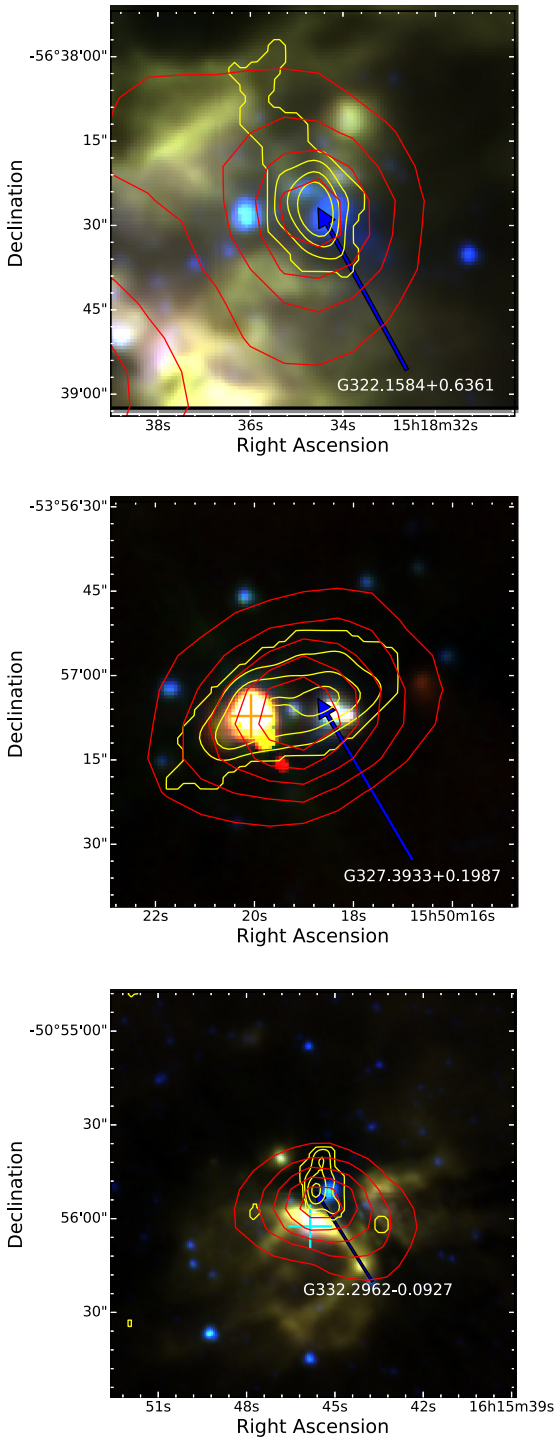

Figure 11. Example GLIMPSE three-colour images of the morphological structure and differences between the three evolutionary stages outlined in this study. The upper panel presents a quiescent clump with no embedded or nearby RMS source, the middle panel presents an ESF field, with an embedded MYSOs, while the lower panel presents an LSF field, where a HII region has developed and started to disrupt its environment. NH_3 (1,1) contours are shown in yellow starting at 3σ increasing in steps of 0.5σ, equivalent to those in Fig. 1. RMS objects are marked with magenta and cyan crosses for MYSOs and H II regions, respectively.

6.3 Comparison of physical parameters

The statistical properties for the entire sample are given in Table 7, and a complete set of maps for each individual field can be found in the appendix.

Throughout this study we have classified each individual source as either early-phase star-forming (ESF) or late-phase star-forming (LSF), and have tried to identify differences between these two classes. The principle basis for this classification system is the difference in morphologies as shown in Figs 6 and 7. The use of maser emission data has additionally allowed the reclassification of regions which appear to be quiescent but are likely to be in a protostellar stage, and therefore are in an early stage of star formation. Although the quiescent clumps are each associated with at least one methanol maser, which are almost exclusively associated with high-mass star formation (e.g. Breen et al. 2011) and are therefore harbouring a protostar, they are yet in an earlier evolutionary stage than the ESF clumps.

We have conducted analysis of the various fitted and derived parameters from the NH_3 observations, and GLIMPSE and ATLAGSAL emissions. ESF and LSF region cumulative distributions were analysed for six of the parameters (luminosity, mass, column density, clump volume, and clump velocity dispersion) in an effort to identify any significant differences and to compare the properties of the two evolutionary samples identified. We have employed the use of a two-sample KS-test for each distribution. The KS-test is used for calculating the probability that two samples are drawn from the same population, and produces a p-value which can be used to reject the null hypothesis. We use a 3σ confidence threshold ($\alpha < 0.0013$) to reject the null hypothesis that any two distributions are drawn from the same parent population. All associated p-values were found to be greater than this confidence value, and so no statistical difference can be seen between the ESF and LSF fields/clumps for any of these parameters.

Temperature and velocity dispersion gradients are common across the sample, ranging from ∼10 to ∼40 K. The peak kinetic temperature measurements of star-forming clumps are in general coincident with an embedded object and decrease towards the edges for the ESF clumps. Many clumps located near LSF sources that have recently broken out of their natal clumps exhibit gradients, with values that peak at the edge closest to the RMS source and decrease with increasing distance from that source. Examples of these two gradient cases seen towards the ESF and LSF clumps are shown in Figs 12 and 13, respectively. These regions will be discussed in the following section.

Feedback from the RMS sources is therefore having a significant impact on the temperature and dynamics of their natal clumps regardless of whether they are still deeply embedded (ESF) or have already started to disrupt their local environment and are starting to emerge from their dust cocoons (LSF). Both classifications have similar median temperatures across the sample, so while the temperature gradients may differ as described above, the absolute values are similar (15–35 K).

Region-wide parameter distributions (luminosity, masses, and column densities) between the two classifications were also investigated for significant differences. It might be expected that the luminosity for LSF regions should be naturally higher as the embedded objects are more luminous whereas ESF clumps are likely to show higher masses and column densities since the natal environments have not started to be dispersed. However, as previously noted, we find no statistical difference between the mass and luminosities of the two classifications in KS-tests. The sizes of individual

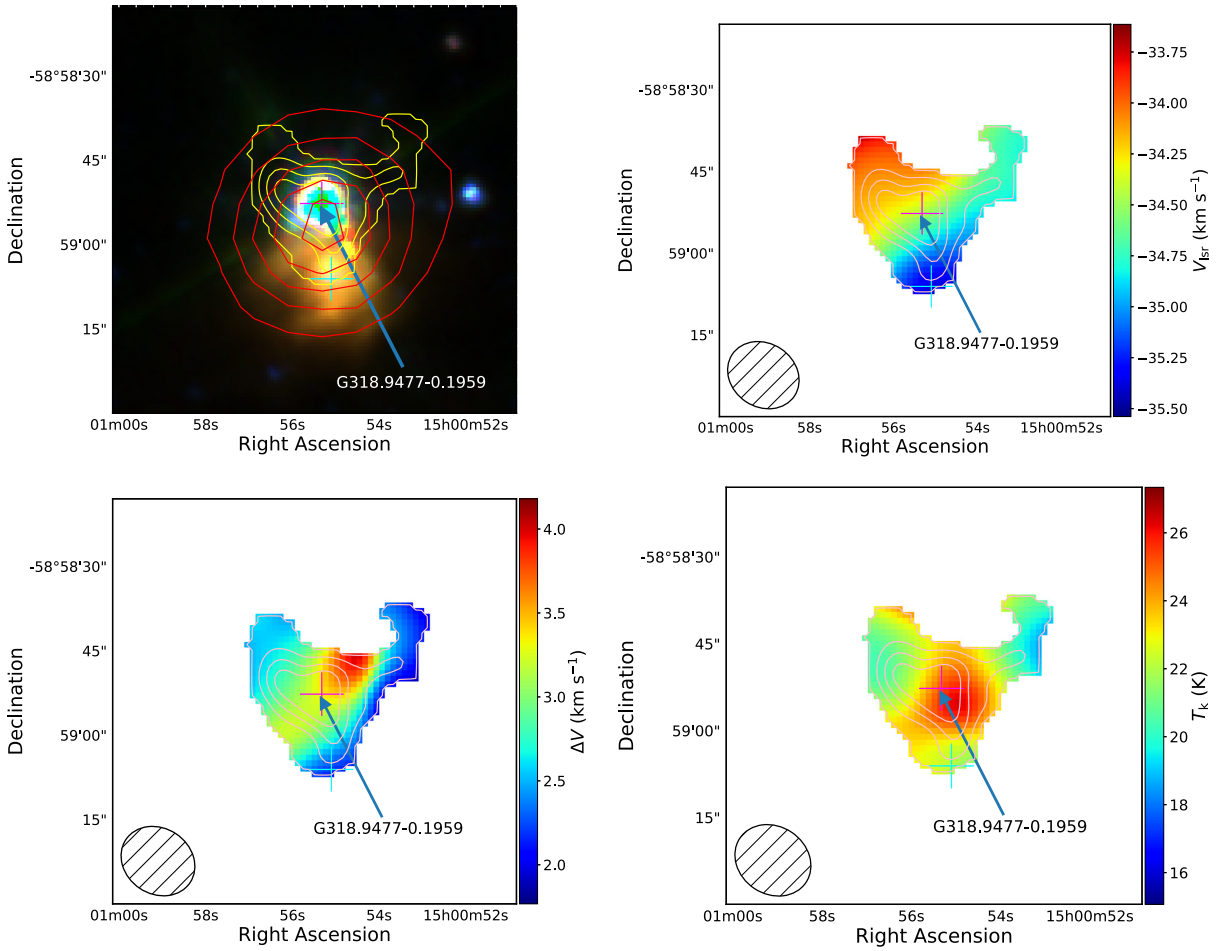

Figure 12. Example maps showing field G318.9480-00.1969. Each panel presents, clockwise from the upper left, three-colour RGB GLIMPSE image overlaid with NH_3 (1, 1) and ATLASGAL dust emission contours in yellow and red, respectively, velocity, kinetic temperature, and velocity dispersion. The contours levels are equivalent to those in Fig. 1. Magenta and cyan crosses mark MYSOs and H II regions, respectively.

clumps has also been compared, and we find that younger clumps tend to be larger than the more evolved material in terms of pixel area (arcsecond^2). The mean luminosity-to-mass (*L*/*M*) ratio for ESF sample is 1.33 with a standard error of 0.03, while the mean LSF ratio is found to be 1.4, with a standard error of 0.05. The median values do also differ by a similar amount. The *L*/*M* ratios are a good indicator of evolutionary stage (increasing *L*/*M* indicates more evolved regions), therefore, from this analysis, it appears that the entire sample covers a narrow evolutionary time-scale. However, analysis of the morphological distribution of the dense gas (as traced by the ammonia) does reveal significant differences between the two evolutionary groups that are not observed in the dust emission maps, which is due to the relatively low spatial resolution of the ATLASGAL survey. The dust emission traces the total column density, rather than just the high-density regions, and so may smooth out any clumpy substructure that is present in the sources.

Urquhart et al. (2014a) found the *L*/*M* ratio to be similar for a large sample of MYSOs and H II regions identified by the RMS survey and concluded that both evolutionary samples were towards the end of the main accretion phase, which is consistent with the finding here. It is also clear that although the H II regions are having a significant impact on the internal structure of their natal clumps and so properties derived from dust emission alone are not very useful to investigate the evolution of these two stages.

6.4 Interesting sources

In the following subsections we present three case studies of interesting regions, along with the associated three-colour RGB GLIMPSE image and parameter maps.

6.4.1 G318.9477 − 0.1959

Fig. 12 shows a selection of parameter maps for a single star-forming region (G318.9480−00.1969). This particular region has a NH_3 (1, 1) SNR of 11.97 and is associated with two sources identified from the RMS survey, one of which is an MYSO (G318.9480 − 00.1969A) that is clearly embedded towards the peak of the ammonia emission. The second is an H II region (G318.9480 − 00.1969B) located towards the southern edge of the NH_3 clump. A single clump (G318.9477 − 0.1959) has been identified in this region by the `FellWalker` algorithm with an aspect ratio of 1.19, and so has a morphology that is fairly circular as seen by the NH_3 (1, 1) emission contours. This clump is located towards the centre of the ATLASGAL dust emission, as expected for an embedded region in the early stages of star formation.

The GLIMPSE RGB image shows a central bright saturated source corresponding to the position of the MYSO, as well as revealing the presence of some diffuse MIR emission coincident

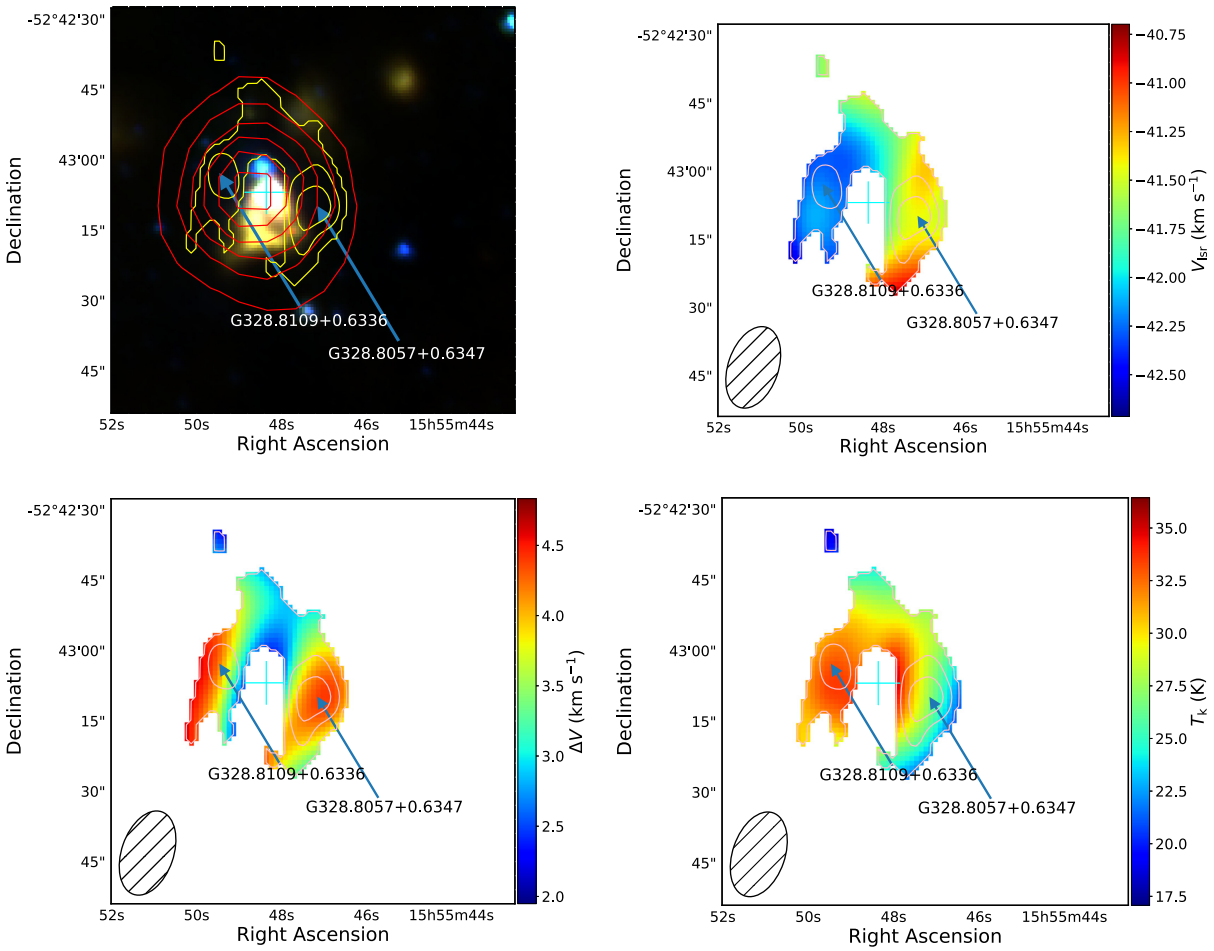

Figure 13. Example maps showing field G328.8074 + 00.6324. Each panel presented is the same as Fig. 12.

with the H II region. Given that the H II region is not associated with any ammonia and is associated with diffuse MIR emission it would appear that the H II region is quite evolved and has started to disperse its surroundings. These two sources dominate the mid-infrared emission in the map. The position of the central object is correlated with an increase in kinetic temperature as expected for an embedded MYSO (see lower right panel of Fig. 12); however, the H II region to the south does not appear to be correlated with a locally elevated gas temperature. This also indicates that it has already dispersed its natal material and is located either slightly in the foreground or background with respect to the clump hosting the MYSO. The line-width maximum is not coincident with either object (see lower left panel of Fig. 12), although the peak values do seem to form an elongated structure running north-west to south-east through the clump roughly centred on the position of the MYSO (see lower left panel of Fig. 12). This is somewhat suggestive of the presence of a bipolar molecular outflow. Similar types of this kind of structure were seen in Paper I in multiple fields (e.g. G010,47+00.03, G011.11−00.40, G013.33−00.03, and G014.61 + 00.02).

This source was studied as G318.9477 − 0.1959 by Navarete et al. (2015) as part of an investigation of the accretion processes in a sample of 353 MYSOs selected from the RMS survey. The study revealed that extended H_2 emission is a good tracer of outflow activity, which is itself a signpost of ongoing accretion processes.

A comparison of this H_2 emission in fig. A296 from Navarete et al. (2015) to the NH_3 maps presented in this study shows that the outflow is directed towards the excavated cavity indicated towards the north-west in Fig. 12; this is also in the direction of the maximum FWHM line width. Closer inspection indicates that there are in fact multiple outflows in this region, likely to be driven by a central cluster. None of these outflows is directly aligned with the FWHM maxima or the excavated cavity, however.

This field is also associated with one methanol and four water masers, all of which are offset less than 0.05 arcsec from the central RMS object (G318.9480 − 00.1969A). The presence of the methanol maser confirms that this region is indeed undergoing high-mass star formation, as these masers are thought to be excited in dense material in an accretion disc by mid-IR pumping from the central source (e.g. De Buizer, Pina & Telesco 2000).

6.4.2 G328.8074 + 00.6324

A second morphologically interesting example is region G328.8074 + 00.6324, shown in Fig. 13. This particular field involves two NH_3-detected clumps which are connected via weaker NH_3 emission, forming a 'horseshoe' shape. These clumps (G328.8057+0.6347 and G328.8109 + 0.6336) have NH_3 (1, 1) SNR values of 7.98 and 5.94, respectively, and aspect ratios of 1.96 and 1.78, so both clumps are fairly elongated in shape. Only one RMS source has been detected in this region

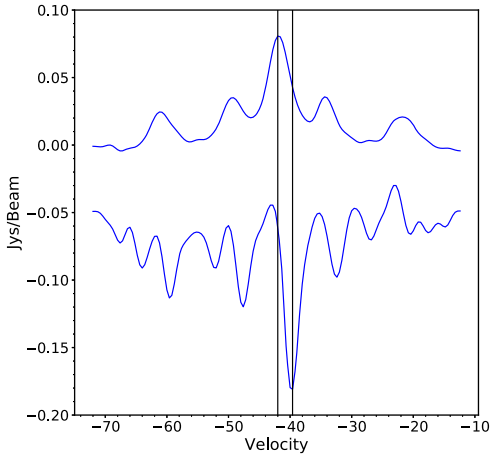

Figure 14. Absorption and emission spectra from field: G328.8074 + 00.6324. The absorption spectrum has been offset by −0.05 Jy. The black lines represent the peaks from the two spectra. The spectra have been smoothed with a 1D Gaussian kernel ($\sigma = 2$).

(G328.8074 + 00.6324). This object has been classified as an H II region by the RMS survey, and lies at the centre of the complex but appears to be removed from any NH_3 emission above the detection threshold. The ATLASGAL dust emission, as with the previous example, is well-correlated with the spatial position of the gas emission and completely encompasses it, with the position of the RMS source approximately coincident with the dust emission. The GLIMPSE image shows multiple evolved stars in the region and a large central IR object corresponding to the H II region, which appears to be somewhat compact with a more diffuse, less intense, envelope. This region is defined as LSF, as the H II region at the centre of the emission is disrupting its environment, and dispersing the dense gas.

The kinetic temperature map shown in Fig. 13 suggests central heating by the RMS source. The kinetic temperature is highest directly around the central H II region and within the central area of the field, while the western edge of G328.8057 + 0.6347 is approximately 10 K cooler, suggesting the feedback from the RMS source is not yet affecting this sector of gas.

The line-width maxima do not correspond well with the temperature distribution: line widths are dominated by non-thermal motions concentrated on the east-west extremities. As with G318.9480 − 00.1969, there appears to be a velocity gradient across the complex, however, a more detailed look at the NH_3 (1, 1) data cube shows that there is NH_3 gas in front of the H II region which is currently in absorption against the bright free–free continuum. Therefore, the H II region is likely to be still enveloped in a shell of dense gas.

Fig. 14 presents two spectra from this region, the first is the average emission spectrum for the NH_3 emission above the 3σ threshold, while the second presents the average absorption averaged over the central nine pixels towards the embedded HII region. The spectral peak velocities are offset by $-2.4\,\mathrm{km\,s^{-1}}$, which indicates that the material in front of the H II region is moving towards us slower than the systemic velocity of the natal clump. This infall motion of material suggests that the clump is still undergoing gravitational collapse. By assuming that the material surrounding the central object is a shell with an average density of $92.5\,\mathrm{M_\odot\,pc^{-3}}$ ($\frac{\mathrm{Mass_{ATLASGAL}}}{\mathrm{Volume_{ATLASGAL}}}$), we have calculated the infall rate for this particular source to be $9.6 \times 10^{-3}\,\mathrm{M_\odot\,yr^{-1}}$. Wyrowski et al. (2016) observed nine massive molecular clumps to search for infall signatures. The mean infall rate was found to be $6.33 \times 10^{-3}\,\mathrm{M_\odot\,yr^{-1}}$ with a standard deviation of $5.95 \times 10^{-3}\,\mathrm{M_\odot\,yr^{-1}}$. The value found for G328.8074 + 00.6324 is similar to this distribution.

We can investigate the stability of the clump using the virial parameter, which is the ratio of virial mass (the mass that can be supported by the internal energy of the clump) and the actual mass of the clump. This is defined as

$$\alpha = \frac{M_{\mathrm{vir}}}{M_{\mathrm{clump}}}, \tag{8}$$

where

$$\left(\frac{M_{\mathrm{vir}}}{\mathrm{M_\odot}}\right) = 161 \left(\frac{R}{\mathrm{pc}}\right) \left(\frac{\Delta v}{\mathrm{km\,s^{-1}}}\right)^2, \tag{9}$$

where R is the radius of the clump and Δv is the line width (Paper I).

An isothermal sphere in hydrostatic equilibrium, supported by equipartition of thermal and magnetic energy, has a critical value of $\alpha_{\mathrm{cr}} = 2$ (Kauffmann, Pillai & Goldsmith 2013). Clumps with a value above this are subcritical and will undergo expansion if not pressure-confined by their local environments. Clumps with values below α_{cr} are supercritical; they are gravitationally unstable, and should be in a state of free-fall unless supported by strong magnetic fields. This particular region has a virial parameter of $\alpha = 2.04$, placing it in the subcritical regime. The error in this value for α is dominated by the ATLASGAL clump mass uncertainty, which is ∼20 per cent (Urquhart et al. 2018). The virial mass also depends on the source distance to calculate the spatial radius of the clump; the error in this distance is ∼17 per cent, obtained from the Reid et al. (2016) model. The difference between α and α_{cr} is relatively small and due to the large errors associated with the virial parameter, the clump could either be sub or supercritical. As the region shows signs of global infall, this potentially means that the central object is beginning to stabilize the inner section of the clump, but the outer layers are undergoing collapse.

6.4.3 G345.5043 + 00.3480

Fig. 15 presents four panels similar to the previous two examples. This source is classified as early star forming, and contains a single MYSO (G345.5043 + 00.3480), offset by less than 1 arcsec (one pixel) from the centre of the NH_3 emission. Line-width and temperature maps have similar distributions, with the maxima located towards the centroid of the clump, with ranges of ∼15–35 K and ∼1.2–5.6 $\mathrm{km\,s^{-1}}$, respectively.

One NH_3 clump has been detected through `FellWalker`, and although another two sources have been detected in the observations, both are smaller than the beam size. The lack of ATLASGAL emission from around these two smaller sources suggests that these are therefore likely to be image artefacts (see Section 3.1). However, while there is no dust emission in this region beyond the main detected clump toward the centre of the field, the NH_3 emission to the north-west of the main clump is coincident with an H_2O maser which can be seen in upper left panel of Fig. 15 and so this source may in fact be a genuine detection.

The GLIMPSE image reveals a large, evolved H II region that lies to the south-west of the main portion of gas emission (see upper left panel of Fig. 15). This H II region has been identified as IRAS 15520−5234 (Walsh et al. 1998; Garay et al. 2006) and is a known radio source. The shape of the clump would imply that the H II region has compressed the dense gas, and subsequently a

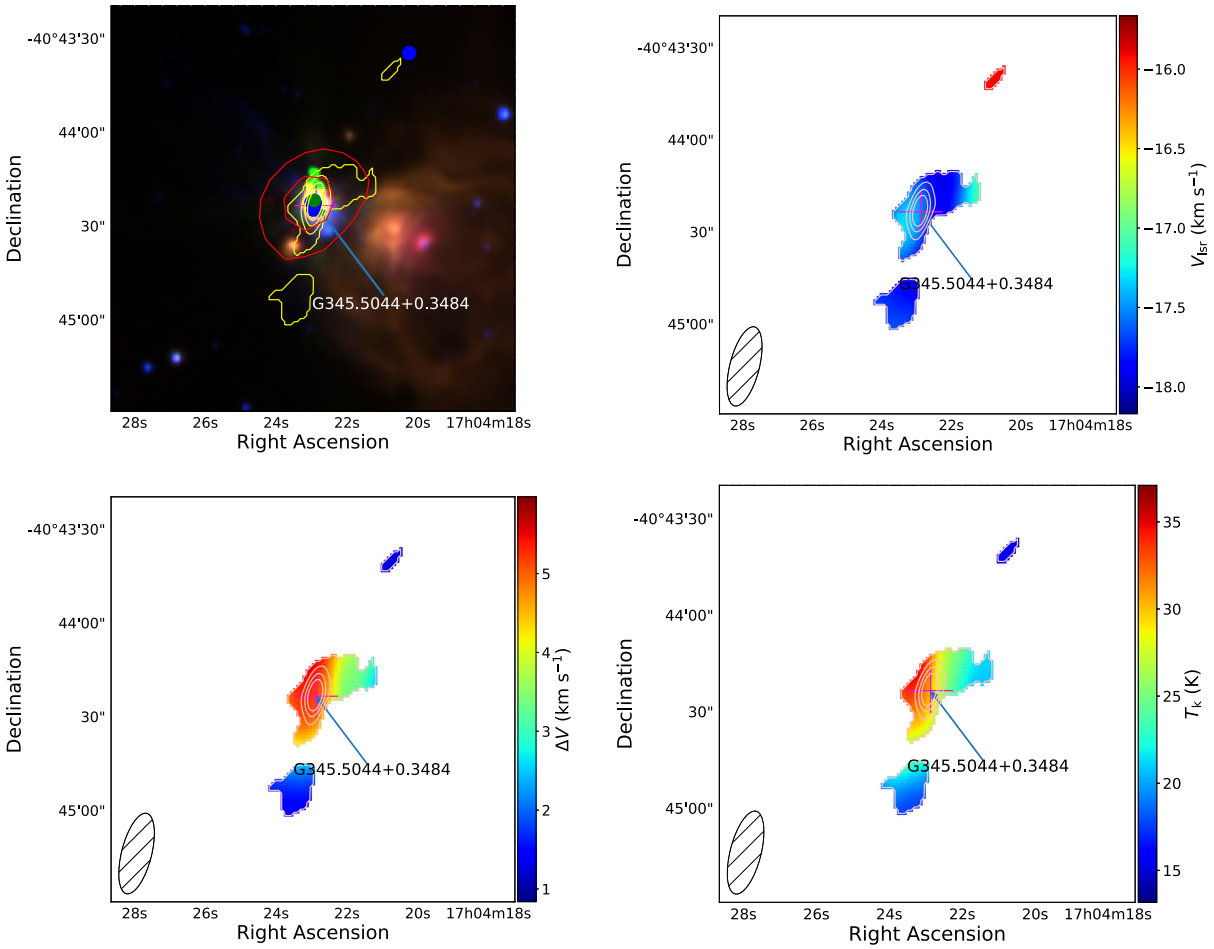

Figure 15. Examples maps showing field G345.5043 + 00.3480. Methanol and H_2O masers have been included in the three-colour GLIMPSE image in with green and blue filled circles, respectively, otherwise each panel presented is the same as Fig. 12.

new star-forming region has been formed on the edge of the region, suggesting an instance of triggered star formation.

This region has the expected temperature and FWHM line-width peaks towards the embedded MYSO, and there is also a very small velocity difference across the central clump, with the smaller source to the north-west having a lower velocity. There appears to be no overlapping infrared or radio emission between these two clumps, although all of the emission appears to be coincident with the edge of the evolved H II region and has similar velocities, and so is likely to be associated.

6.5 Triggered star formation

Elmegreen (1992) proposed a model of triggered star formation, wherein an ionization shock front produced by the expansion of H II regions created by one group of massive stars provides the external pressure to compress adjacent material in a molecular clouds, thereby inducing subsequent generations of massive stars to form. This mechanism is thought to play a significant role in the evolution of massive star forming regions (e.g. Thompson et al. 2012).

As discussed previously, methanol masers are located at the sites of high-mass star formation, while H_2O masers are sensitive to shocked material. By using maser positions and the likely presence of an H II region (which can be inferred through the morphology of extended 8 μm emission), multiple regions presented in this study are consistent with triggered star formation. As H II regions expand into nearby molecular material, they begin to compresses this matter which could form future generations of high-mass stars. The incorporated maser emission data helps to refine this picture as both methanol and water maser emission is known to be coincident with star formation.

Fig. 16 presents three regions which appear to contain examples of triggered star formation at different stages. The top panel of Fig. 16 shows a relatively early and compact H II region to the north-west of the NH_3 emission. It can be seen that two methanol masers are present within the dense material traced by the NH_3 in different locations, implying two protostellar cores are embedded within the environment. This is potentially due to the influence of the nearby H II region which suggests that this material is undergoing shocks. The middle panel of Fig. 16 presents the same effect more conclusively. The H II region towards the south is clearly having an impact on the dense material and is dispersing its environment, indicated by the appearance of multiple NH_3 clumps on the edges of the radiation. The central clump also has a string of H_2O masers along this boundary, which suggests that this material is undergoing shock. Two methanol masers are located behind these H_2O masers, again implying the presence of high-mass protostellar cores, which are likely to have formed due to the compression of gas as the H II region expands towards it. The lower panel of Fig. 16 presents a more diffuse H II region in the south-west which seems to be in

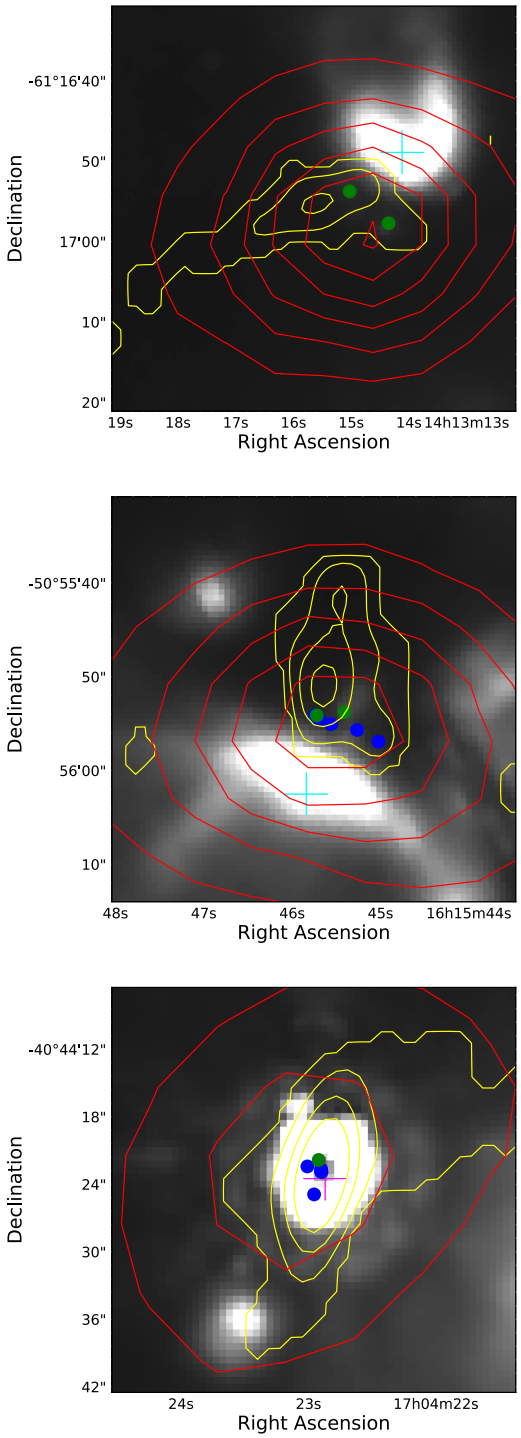

Figure 16. Three GLIMPSE 8 μm images presenting regions of possible triggered star formation. Each panel presents an 8 μm image overlaid with NH_3 and ATLASGAL emission contours in yellow and red, respectively. The contours levels are equivalent to those in Fig. 1. MYSOs and H II regions identified by the RMS survey are show with magenta and cyan crosses, respectively. Methanol and water maser positions are marked with green and blue filled circles, respectively.

a later evolutionary stage. A MYSO has already formed within the gas and dust emission, which has been subjected to the effects of the nearby H II region. This MYSO is associated with two methanol masers and 10 H_2O masers.

These three regions show the effect that H II regions have on their local environment and the likelihood that they can cause triggered star formation and produce future generations of stars. The use of the classification system presented in this paper creates a difficulty in assigning these types of regions, as they display both qualities of ESF and LSF fields. While HII regions are present and are impacting on their local environment, the presence of a large number of maser detections implies protostellar objects in an initial stage of formation.

7 CONCLUSIONS

We have mapped 34 fields using the NH_3 (1, 1) and (2, 2) inversion transitions. We have used the `FellWalker` algorithm with a threshold value of 3σ to identify 44 clumps distributed among these regions. No statistical differences are found between clumps classified as early star-forming or late star-forming when using a two sample KS-test. The early star formation (ESF) star-forming clumps do generally exhibit elevated temperatures, while the late star formation (LSF) counterparts have larger line widths. Most ESF clumps have been previously identified by as MYSOs while the majority of LSF clumps are associated with H II regions. Physical parameters have been extracted from complementary surveys such as ATLASGAL and GLIMPSE legacy surveys. Masses for the fields range between a few hundred to over 10 000 $M_\odot$ and luminosities range between $\sim 10^3$ and $\sim 10^6$ $L_\odot$.

We have used these data to construct a rudimentary evolutionary sequence of proposed massive star formation based on the morphology of their associated high-density gas. ESF fields generally have RMS objects which are found towards the centre of centrally condensed coherent clumps, while the embedded objects within LSF regions are not coincident with dense gas but are generally found to be surrounded by multiple fragments. The higher level of fragmentation seen towards the LSF clumps is consistent with an expectation of association with more evolved and more luminous H II regions that are disrupting and 'burning out from' their natal clumps. The clump-averaged physical properties of these two samples are not statistically different from each other (mass, luminosity, temperatures, and line widths), although the structure of the dense gas is very different, which may indicate that the formation of the H II region has a much more significant impact on the overall structure of natal clump than on its physical properties.

We find that 31 methanol masers associated with 34 fields and 52 water masers are associated 21 fields. The majority of both types of masers are found towards ESF fields. The detection rates for water masers for the ESF and LSF field are 89 per cent and 25 per cent, respectively, with a similar average number of spots detected in both ESF and LSF fields. The detection rates for methanol masers are 72 and 44 per cent for the ESF and LSF fields, respectively. The reason for the significantly lower detection rates towards the LSF clumps is likely to be linked to the disruption of natal clumps by the expansion of the H II regions.

Triggered star formation appears to be present in three of the observed regions. The 8 μm images of these sources all show the presence of nearby H II regions that show evidence of affecting the dense gas as traced by NH_3 emission seen towards these sources. A large number of methanol and water masers are found to be coincident with these regions revealing that these nearby H II regions

are not only having a significant impact on their local environments but are also appears to be having an a direct influence star formation in the surrounding dense gas.

ACKNOWLEDGEMENTS

The authors would like to thank the staff of the ATCA (Australia Telescope Compact Array) for their assistance during the preparation and execution of these observations. S. J. Billington wishes to acknowledge an STFC (Science and Technology Funding Council) PhD studentship for this work. We have used the collaborative tool Overleaf available at: https://www.overleaf.com/.

REFERENCES

Battersby C., Ginsburg A., Bally J., Longmore S., Dunham M., Darling J., 2014, ApJ, 787, 113
Benjamin R. A. et al., 2003, PASP, 115, 953
Berry D. S., 2015, Astron. Comput., 10, 22
Breen S. L., Ellingsen S. P., Caswell J. L., Green J. A., Fuller G. A., Voronkov M. A., Quinn L. J., Avison A., 2011, ApJ, 733, 80
Caswell, J. L. E., 2010, MNRAS, 404, 1029
Chambers E. T., Jackson J. M., Rathborne J. M., Simon R., 2009, ApJS, 181, 360
Chira R.-a., Beuther H., Linz H., Schuller F., Walmsley C. M., Menten K. M., Bronfman L., 2013, A&A, 552, A40
Churchwell E. et al., 2009, PASP, 121, 213
Claussen M. J., Wilking B. A., Benson P. J., Wootten A., Myers P. C., Terebey S., 1996, ApJS, 106, 111
Contreras Y. et al., 2013, A&A, 549, A45
Cooper H. D. B. et al., 2013, MNRAS, 430, 1125
Csengeri T. et al., 2014, A&A, 565,A75
Cutri R. M. et al., 2003, 2MASS All Sky Catalog of Point Sourcesin The IRSA 2MASS All-Sky Point Source Catalog, NASA/IPAC Infrared Science Archive
Cyganowski C. J. et al., 2008, AJ, 136, 2391
De Buizer J. M., Pina R. K., Telesco C. M., 2000, ApJS, 130, 437
De Buizer J. M., Watson A. M., Radomski J. T., Piña R. K., Telesco C. M., 2002, ApJ, 564, L101
Deharveng L. et al., 2010, A&A, 523, A6
Dickinson D. F., 1976, ApJS, 30, 259
Dunham M. K., Rosolowsky E., Evans, II N. J., Cyganowski C., Urquhart J. S., 2011, ApJ, 741, 110
Eden D. J. et al., 2017, MNRAS, 2183, 2163
Elmegreen B. G., 1992, Star Formation in Stellar Systems. University of Cambridge Press, Cambridge, p. 381
Elmegreen B. G., Scalo J.,2004, ARA&A, 42, 211
Fazio G. G. et al., 1998, in Fowler A. M., ed., Proc. SPIE Conf. Ser. Vol. 3354, Infrared Astronomical Instrumentation. SPIE, Bellingham, p. 1024
Forster J., Caswell J. L., 1999, A&AS, 137, 43
Friesen R. K., Di Francesco J., Shirley Y. L., Myers P. C., 2009, ApJ, 697, 1457
Garay G., Brooks K. J., Mardones D., Norris R. P., 2006, ApJ, 651, 914
Ginsburg A., Mirocha J., 2011, Astrophysics Source Code Library, 1109.001
Green J. A. et al., 2009, MNRAS, 392, 783
Ho P., Haschick A., Vogel S., Wright M., 1983, AJ, 295
Kauffmann J., Pillai T., Goldsmith P. F., 2013, ApJ, 779
Kennicutt R. C., 2005, in Cesaroni R., Felli M., Churchwell E., Walmsley M., eds, Proc. IAU Symp. 227, Massive Star Birth: A Crossroads of Astrophysics. Cambridge University Press, Cambridge, 3
Kurtz S., Churchwell E., Wood D. O. S., 1994, ApJS, 91, 659
Longmore S. N. et al., 2017, MNRAS, 470, 1462
Lumsden S. L., Hoare M. G., Urquhart J. S., Oudmaijer R. D., Davies B., Mottram J. C., Cooper H. D. B., Moore T. J. T., 2013, ApJS, 208, 11
Mangum J. G., Wootten A., Mundy L. G., 1992, ApJ, 388, 467
Minier V., Ellingsen S. P., Norris R. P., Booth R. S., 2003, A&A, 403, 1095
Miranda L. F., Gómez Y., Anglada G., Torrelles J. M., 2001, Nature, 414, 284
Moore T. J. et al., 2015, MNRAS, 453, 4264
Mottram J. C., Hoare M. G., Lumsden S. L., Oudmaijer R. D., Urquhart J. S., Sheret T. L., Clarke A. J., Allsopp J., 2007, A&A, 476, 1019
Mottram J. C. et al., 2011a, ApJ, 730, L33 +
Mottram J. C. et al., 2011b, A&A, 525, A149
Navarete F., Damineli A., Barbosa C. L., Blum R. D., 2015, MNRAS, 450, 4364
Perault M. et al., 1996, A&A, 315, L165
Pillai T., Wyrowski F., Carey S. J., Menten K. M., 2006, A&A, 450, 569
Price S. D., Egan M. P., Carey S. J., Mizuno D. R., Kuchar T. A., 2001, AJ, 121, 2819
Purcell C. R. et al., 2012, MNRAS, 426, 1972
Ragan S. E., Bergin E. A., Wilner D., 2011, ApJ, 736
Reid M. J. et al., 2009, ApJ, 700, 137
Reid M. J., Dame T. M., Menten K. M., Brunthaler A., 2016, ApJ, 823, 1
Rosolowsky E. W., Pineda J. E., Foster J. B., Borkin M. A., Kauffmann J., Caselli P., Myers P. C., Goodman A. A., 2008, ApJS, 175, 509
Rosolowsky E., Ginsburg A., Ellsworth-Bowers T., 2010, ASPC, 438, 76
Sault R. J., Teuben P. J., Wright M. C. H., 1995, in Shaw R. A., Payne H. E., Hayes J. J. E., eds, ASP Conf. Ser. Vol. 77, Astronomical Data Analysis Software and Systems IV. Astron. Soc. Pac., San Francisco, p. 433
Schuller F. et al., 2009, A&A, 504, 415
Sridharan T. K., Beuther H., Schilke P., Menten K. M., Wyrowski F., 2002, ApJ, 566, 931
Swift J. J., Welch W. J., Di Francesco J., 2005, ApJ, 620, 823
Thompson M. A., Urquhart J. S., Moore T. J. T., Morgan L. K., 2012, MNRAS, 421, 408
Urquhart J. S., Busfield A. L., Hoare M. G., Lumsden S. L., Clarke A. J., Moore T. J. T., Mottram J. C., Oudmaijer R. D., 2007a, A&A, 461, 11
Urquhart J. S., Thompson M. a., Morgan L. K., Pestalozzi M. R., White G. J., Muna D. N., 2007b, A&A, 467, 1125
Urquhart J. S. et al., 2007c, A&A, 474, 891
Urquhart J. S. et al., 2008, A&A, 487, 253
Urquhart J. S., Morgan L. K., Thompson M. a., 2009a, A&A, 497, 789
Urquhart J. S. et al., 2009b, A&A, 501, 539
Urquhart J., Hoare M., Moore T., Morgan L., Figura C., 2010, Probing the environments of young massive stars. ATNF Proposal, ATNF, Australia
Urquhart J. S. et al., 2011, MNRAS, 418, 1689
Urquhart J. S. et al., 2012, MNRAS, 420, 1656
Urquhart J. S. et al., 2013a, MNRAS, 431, 1752
Urquhart J. S. et al., 2013b, MNRAS, 435, 400
Urquhart J. S. et al., 2014a, A&A, 568, A41
Urquhart J. S., Figura C. C., Moore T. J. T., Hoare M. G., Lumsden S. L., Mottram J. C., Thompson M. A., Oudmaijer R. D., 2014b, MNRAS, 437, 1791
Urquhart J. S. et al., 2014c, MNRAS, 443, 1555
Urquhart J. S. et al., 2015a, MNRAS, 452, 4029 (Paper I)
Urquhart J. S. et al., 2015b, MNRAS, 446, 3461
Urquhart J. S. et al., 2018, MNRAS, 473, 1059
Walmsley C. M., Ungerechts H., 1983, A&A, 122, 164
Walsh A. J., Burton M. G., Hyland A. R., Robinson G., 1998, MNRAS, 301, 640
Walsh A. J. et al., 2011, MNRAS, 416, 1764
Walsh A. J., Purcell C. R., Longmore S. N., Breen S. L., Green J. A., Harvey-Smith L., Jordan C. H., Macpherson C., 2014, MNRAS, 442, 2240
Wienen M., Wyrowski F., Schuller F., Menten K. M., Walmsley C. M., Bronfman L., Motte F., 2012, A&A, 544, A146
Wilson W. E. et al., 2011, MNRAS, 416, 832
Wood D. O. S., Churchwell E., 1989, ApJ, 340, 265
Wyrowski F. et al., 2016, A&A, 149, 1
Zinnecker H., Yorke H. W., 2007, ARA&A, 45, 1

SUPPORTING INFORMATION

Supplementary data are available at *MNRAS* online.

Table 3. `FellWalker` source catalogue for detected clumps.
Table 6. Detected NH_3 clump parameters.
Appendix A. Online Material.

Please note: Oxford University Press is not responsible for the content or functionality of any supporting materials supplied by the authors. Any queries (other than missing material) should be directed to the corresponding author for the article.

This paper has been typeset from a TEX/LATEX file prepared by the author.